Heliyon 5 (2019) e02721

Contents lists available at ScienceDirect

Heliyon

journal homepage: www.heliyon.com

Research article

U–Pb geochronology and Hf isotope data from the Late Cretaceous Mawat ophiolite, NE Iraq

Heider Al Humadi [a,b,*], Markku Väisänen [a], Sabah A. Ismail [c], Jaakko Kara [a], Hugh O'Brien [d], Yann Lahaye [d], Marja Lehtonen [d]

[a] Department of Geography and Geology, 20014 University of Turku, Finland
[b] Department of Applied Geology, College of Sciences, University of Babylon, Iraq
[c] Department of Applied Geology, College of Sciences, University of Kirkuk, Iraq
[d] Geological Survey of Finland, 02151 Espoo, Finland

ARTICLE INFO

Keywords:
Earth sciences
Geochemistry
Geology
Mawat ophiolite
U–Pb geochronology
Felsic dyke
Gabbro
Hf isotopes

ABSTRACT

The Mawat ophiolite, NE Iraq, is one of the Neo-Tethyan ophiolites within the Iraqi Zagros orogen. It consists of many metre-to kilometre-sized tectonic slices of serpentinized dunite, peridotite, gabbro, basaltic rocks and associated oceanic metasediments. Felsic intrusions crosscut the ophiolite. We present U–Pb zircon and monazite ages and Hf zircon isotopes from two crosscutting felsic dykes and a gabbro from the mantle section of the ophiolite. Zircons from the felsic dykes contain spongy domains and xenotime and monazite inclusions. They give ages from 222 to 46 Ma. The age range is interpreted to be caused by secondary processes such as radiogenic Pb mobility and Pb loss. The monazite age of 94.6 ± 1.2 Ma is considered to give a crystallisation age of the felsic dykes. The gabbro zircons give ages between 81 to 38 Ma of which the two oldest grains give the weighted average age of 81.2 ± 2.5 Ma which we interpret to be the crystallisation age of the gabbro. The zircon initial ε_{Hf} values in the felsic dykes are negative (averages -2.7 and -3.1) while they in the gabbro are positive (average + 3.5), indicating that the felsic magma comes from an older source while the mafic magma comes from a juvenile one. Two mafic units of different ages were identified: the older unit is cut by the 95 Ma felsic dykes and the younger one is represented by the 81 Ma gabbro located within a thrust zone. The youngest ages of 40 Ma are considered to be related to crustal extension.

1. Introduction

During the closure of the Neo-Tethyan ocean numerous oceanic fragments (ophiolites) were obducted in the Tethyan suture zone. The ophiolites now work as natural laboratories from where the information of the plate tectonic paradigm is partly based on. The classical ophiolites in the eastern Mediterranean have been studied intensively (e.g., Pearce, 1980; Dilek and Thy, 2009) as are the Oman ophiolites in the Zagros orogen (e.g., Hacker, 1994; Rollinson, 2015 and references therein).

In a collision between the Arabian and Eurasian plates an accretionary complex, the Zagros orogen, was formed. In the central part of the Zagros orogen in Iran and Iraq, long term systematic work on ophiolites has been less active. Therefore, much of the elementary information, e.g., modern geological maps and geochemical data, are locally missing. However, especially in Iran, much progress has been recently achieved (c.f., Moghadam and Stern, 2014 and references therein) by isotopic and geochemical studies in Kermanshah (Ao et al., 2016), in Neyriz (Monsef et al., 2018) and in the metamorphic-sedimentary Sanandaj-Sirjan zone (Zhang et al., 2018). In Iraq, a few recent studies have clarified the role of ophiolites for the Zagros orogen (e.g., Aswad et al., 2011; Ali et al., 2013; Ismail et al., 2017).

However, in spite of recent progress, the geodynamic role of the Neo-Tethyan ophiolites is still highly controversial (Ao et al., 2016).

In this study we report single-grain laser-ablation U–Pb ages of zircons and monazites from two felsic dykes and a gabbro hosted in the mantle section of the Mawat ophiolite in the Kurdistan region, NE Iraq, to obtain new basic data for the geotectonic models, These were also analysed for Hf zircon isotopes in order to trace sources of the magmas.

2. Geological setting

Mesozoic ophiolites in the western and eastern Mediterranean are

* Corresponding author.
E-mail address: heialm@utu.fi (H. Al Humadi).

https://doi.org/10.1016/j.heliyon.2019.e02721
Received 27 December 2018; Received in revised form 26 June 2019; Accepted 22 October 2019

A

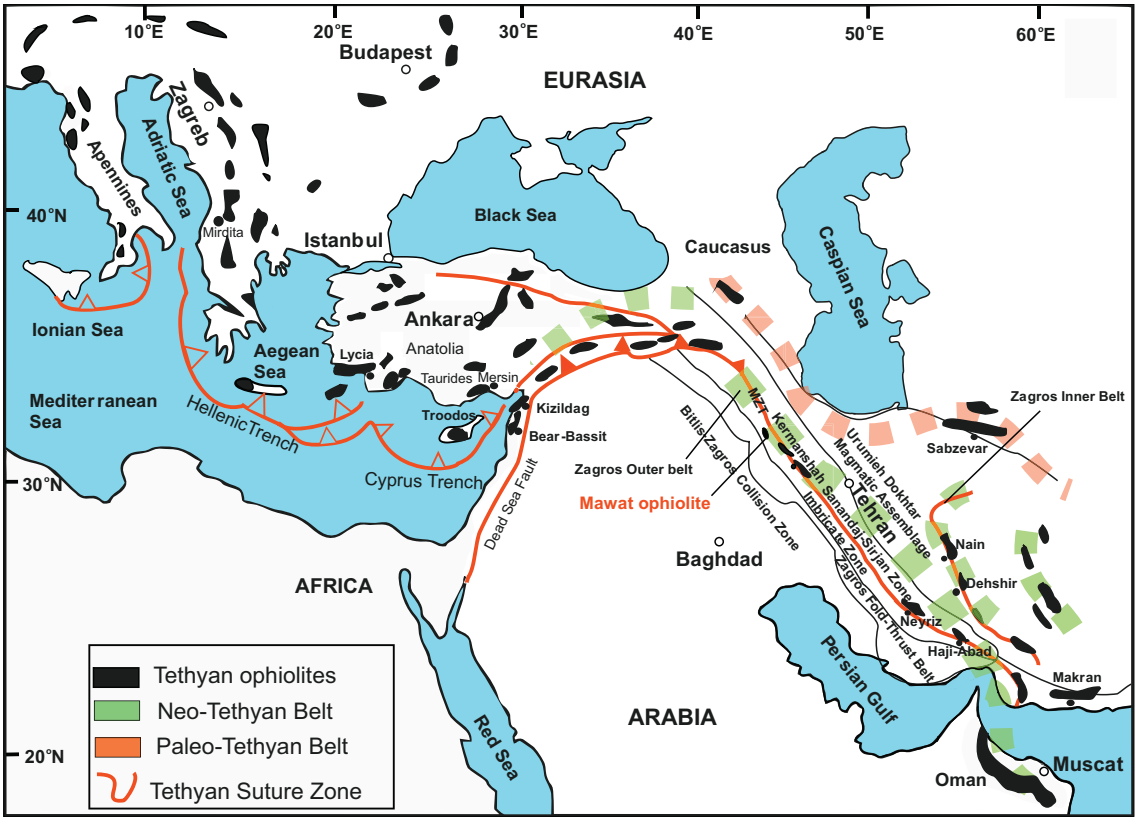

B

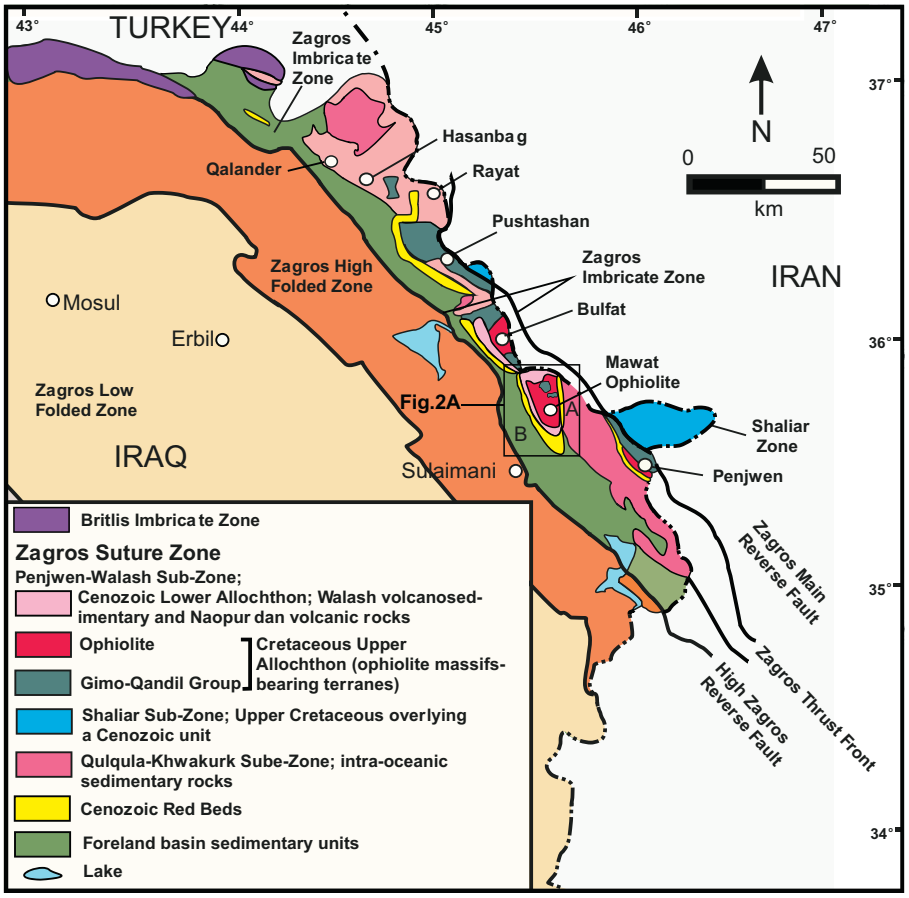

(caption on next page)

remnants of the Neo-Tethys Ocean. They formed during the ongoing collision of the Afro-Arabian and Eurasian continents. These ophiolites were divided into two groups: the Jurassic ophiolites in the west, and the Cretaceous ophiolites in the east (Abbate et al., 1980). The Mesozoic ophiolites occur in four belts: the Jurassic Alpine-Apennine belt in the western Mediterranean, the Jurassic Dinaride-Hevenide belt in western Balkan, the Jurassic-Cretaceous belt in eastern Greece and central Turkey, and the late Cretaceous belt in southern Turkey, Cyprus, northeastern Syria extending to northeast Iraq and northwest Iran and Oman (Lagabrielle and Cannat, 1990; Smith, 1993; Dilek et al., 2007; Dilek and Thy, 2009, Fig. 1A). The late Cretaceous ophiolites including the pre-Arabian ophiolites along the Bitlis-Zagros suture zone represent relicts of the southern Neo-Tethyan oceanic lithosphere obducted by a series of collisions of intra-oceanic arc-trench system and the continental margins (Dilek et al., 1999). The Paleozoic ophiolites are preserved in the southwestern margin of Eurasia in Iran, Turkey, Caucasus, Turkmenistan, Afghanistan and Tibet. They were formed during opening and closing of the Paleo-Tethys Ocean. The Paleozoic ophiolites occur mainly in the northern part of Iran and are related to later opening of the Paleo-Tethys Ocean during the Ordovician-Silurian time (Moghadam and Stern, 2014, Fig. 1A).

2.1. Zagros Orogenic Belt

The Zagros Orogenic Belt (ZOB) is a young continental convergence zone located along the boundary of the Arabian and Eurasian Plates. This belt represents the central part of the Alpine-Himalayan orogenic system starting from the East Anatolian Fault in southeastern Turkey and continuing through northeastern Iraq to the Makran Subduction Zone in southern Iran (Falcon, 1974; Dercourt et al., 1986; Alavi, 1994; Hessami, 2002). The ZOB formed as a result of the closure of the Neo-Tethys Ocean during three tectonic events: subduction of the Neo-Tethys Ocean beneath central Iran in Cretaceous, tectonic emplacement of ophiolites over the Afro-Arabian passive continental margin in the late Cretaceous, and collision of the Arabian plate with the Iranian microcontinent in the Cenozoic time (Alavi, 1994).

The ZOB comprises four parallel tectonic subdivisions from SW to NE (Fig. 1A): 1) the Zagros Fold-Thrust Belt, 2) the imbricate zone, 3) the Sanandaj-Sirjan zone, and 4) the Urumieh-Dokhtar magmatic assemblage (Alavi, 1994). The Sanandaj-Sirgan zone represents the metamorphic/deformation belt of the ZOB (Hassanzadeh and Wernicke, 2016). It is composed mainly of metamorphic and plutonic rocks and widespread Mesozoic volcanic rocks (Mohajjel et al., 2003). The imbricate zone in the Iraqi section is a NW-SE trending 15–25 km wide and 250 km long belt. It consists of imbricate tectonic slices of Qulqula radiolarite, Mesozoic ophiolites and Cretaceous-Tertiary sedimentary rocks. Three tectonic subzones are identified within the Zagros suture zone (Fig. 1B):

(i) Qulqula-Khwarkuk Zone has deep water margin sediments (radiolarian chert and limestone).
(ii) Penjwen-Walash Zone represents the central part of the Neo-Tethys consisting of two thrust sheets: a) Cenozoic Naupordan-Walash Group is the lower allochthon comprising unmetamorphosed Paleogene fore-arc and volcanic arc rocks (Bulfat ophiolite) formed during the closure of the Neo-Tehthys Ocean (Aswad et al., 2016), and b) Cretaceous Gimo-Qandil Group is the upper allochthon (ophiolite bearing terrane) containing metamorphosed mafic volcanic rocks and sediments. The upper allochthon was thrust over the lower allochthon and these two were juxtaposed and merged together (Penjwen-Walash Zone). The Penjwen-Walash Zone was thrust over the Red beds (Aswad et al., 2011; Ali et al., 2012)
(iii) Shalair Zone is part of the Sanandj-Sirjan zone, consisting of pre-Cretaceous metamorphic basement.

The Main Zagros Thrust divides the Zagros ophiolites into the Inner and Outer Zagros ophiolitic belts (Moghadam and Stern, 2011). Moghadam and Stern (2015) consider the Iraqi-Iranian Zagros ophiolites belong to the Outer Zagros ophiolitic belt located south of the Main Zagros Thrust. These ophiolites along the Iraq-Iran border formed by subduction of the Neo-Tethyan Ocean toward the east and northeast during the early Cretaceous time (106-92 Ma; ^{40}Ar-^{39}Ar age of igneous kaersutite; the Hasanbag ophiolite; Ali et al., 2012). These ages overlap those of the Iranian ophiolites (98 Ma; U–Pb zircon Kermanshah; Moghadam et al., 2011) and (95-85 Ma; phengite ^{40}Ar-^{39}Ar age of blueschists, the Haji Abad ophiolite; Agard et al., 2006). In contrast, the Inner Zagros ophiolites are apparently older than the Outer Zagros ones. The U–Pb zircon ages for the Nain ophiolite is 103-101 Ma (Rahmani et al., 2007) and for the Dehshir ophiolite 101-99 Ma (Moghadam et al., 2010).

The Iraqi Zagros segment preserves several phases of subduction, collision and, post-collisional extension in association with the extensive Cenozoic magmatism. In Iraq, ophiolites within the Zagros suture zone are distributed discontinuously, marking the boundary between the Arabian and Eurasian continental plates. These ophiolites represent remnants of the southern Neo-Tethyan oceanic crust. They were obducted in two major episodes during the late Cretaceous and Paleogene colliding intra-oceanic arc-trench systems with the Arabian continental margin (Ismail and Carr, 2008; Ismail et al., 2014). The Mawat, Penjween and Pushtashan ophiolites are Mesozoic. The mélange-type assemblages are represented by Rayat (Arai et al., 2006; Ismail et al., 2009), and Qalander (Ismail and Al-Chalabi, 2006) occurrences occurring within the Eocene thrust sheets of Walash-Naopurdan Groups. The Neo-Tethyan ophiolites from the Zagros suture zone (e.g. the Pushtashan ophiolite; Ismail et al., 2017, and the Hasanbag ophiolite; Ali et al., 2012) indicate late Cretaceous ages.

The uppermost part of the Mawat ophiolite consists of volcanic and sedimentary rocks of the Gimo group in the north, whereas in the east the N–S and in the west the NW-SE trending thrust faults have complicated the stratigraphy. The Mawat ophiolite is now located between two thrust sheets, the Walash and Naopurdan Groups, transported from the east and west (Fig. 2B).

2.2. Mawat ophiolite

The Mawat ophiolite is one of the largest, well-preserved and best-exposed fragments of the Neo-Tethyan oceanic lithosphere in Iraqi Zagros suture zone. It includes mantle peridotites and thick (~2500m) crustal gabbros. Minor dioritic lenses and diabasic dikes and late stage plagiogranite dykes intrude the peridotites (Mirza and Ismail, 2007; Ismail et al., 2010; Mohammad and Qaradaghi, 2016; Mohammad and Cornell, 2017). The ophiolite covers >250 km^2 in elevated area with significant topographic relief within the Iraqi Zagros belt (Fig. 2A).

The relatively complete lithostratigraphic sequence is preserved but is missing the sheeted dykes. Harzburgite, lherzolite, dunite and pyroxenite dykes are the main constituents of the Mawat mantle sequence, which is in tectonic contact with the underlying Paleogene Walash-Naopurdan series. Peridotites are serpentinized near the thrust and generally the alteration decreases with distance from the thrust zone. Chromitites and dunites are abundant in the central part of the ophiolite (Ismail et al., 2010). The main components of the Mawat crustal sequence are mainly

Fig. 1. (A) Distribution of Tethyan ophiolites and suture zones in the eastern Mediterranean and the Zagros Orogenic Belt (modified from Dilek et al., 2009). Tectonic units are modified from (Alavi, 1994). Neo- and Paleo-Tethyan belts, location of the Mawat ophiolite, the Zagros Outer and Inner Belts and MZT (Main Zagros Thrust) are indicated. (B) Regional tectonic map of NE Iraq (Kurdistan region), showing the major tectonic subdivisions (modified from Al-Kadhimi et al., 1996). The tectonic zones and boundaries are modified from Al-Qayim et al. (2012).

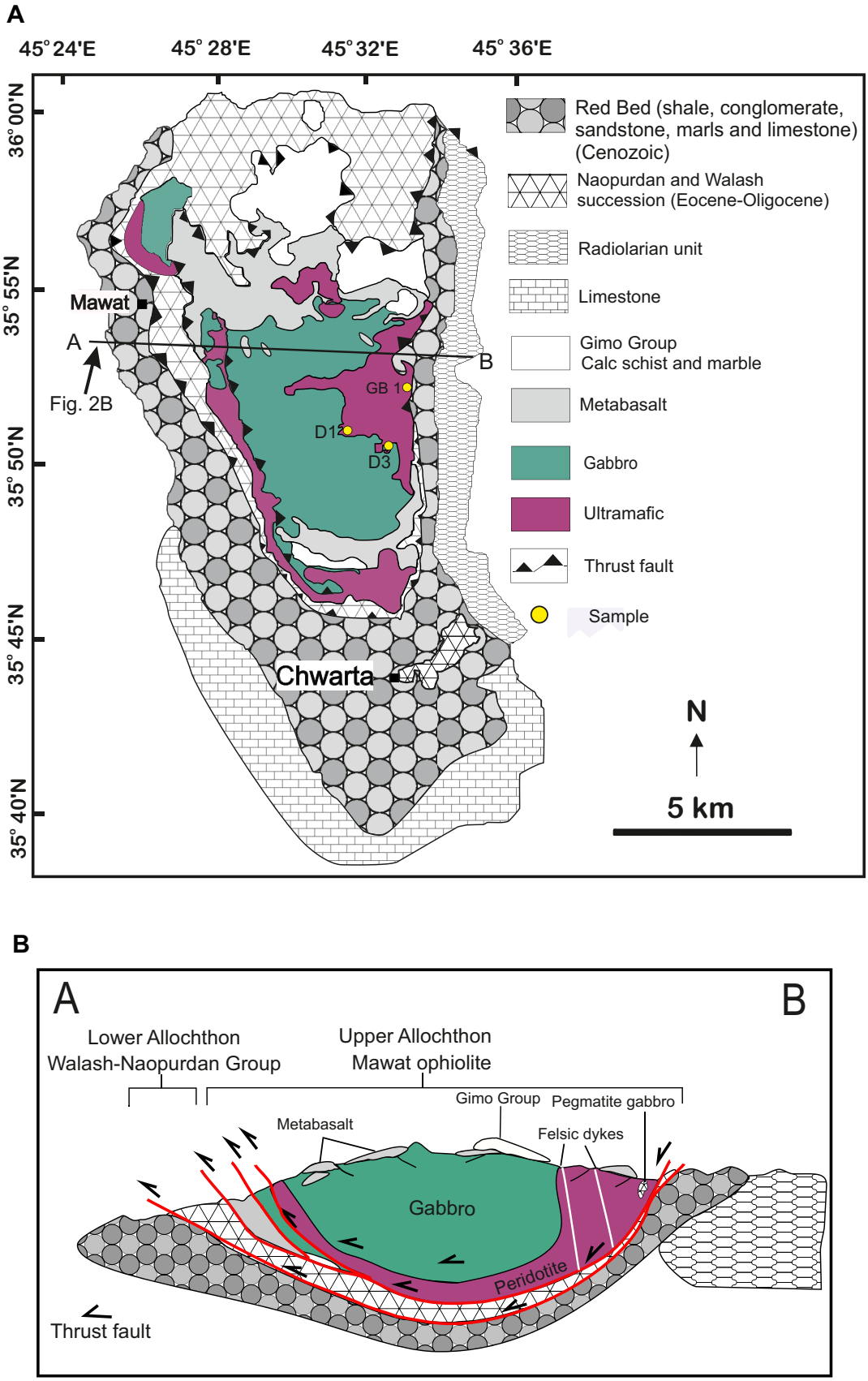

Fig. 2. (A) Simplified geological map of the Mawat ophiolite (modified from Aziz, 2008). (B) Simplified cross-section of the Mawat ophiolite along the traverse A-B (modified from Jassim and Goff, 2006). For location and legend see Fig. 2A.

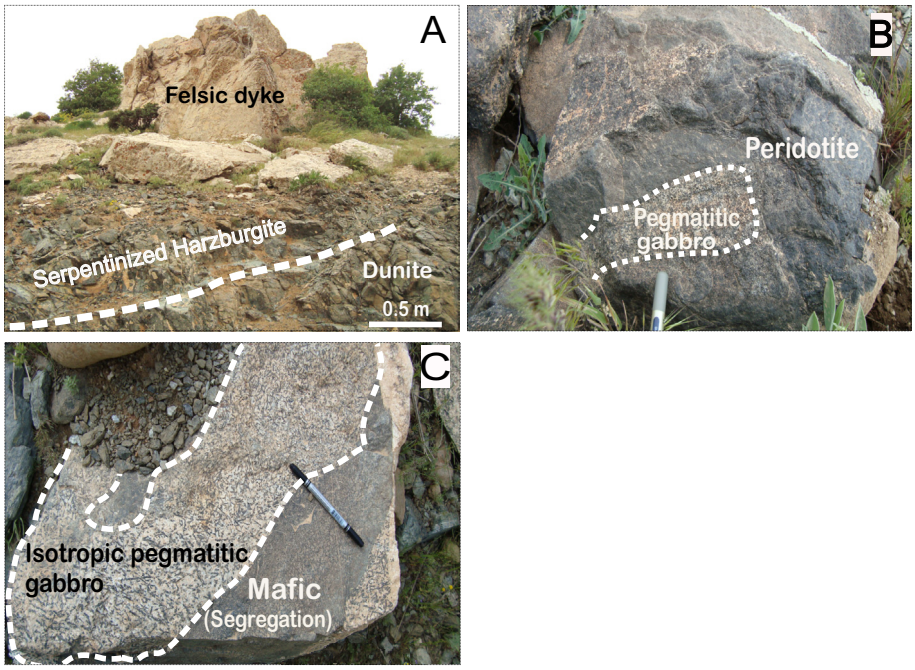

Fig. 3. Field photographs from the Mawat ophiolite, showing (A) Felsic dyke intruding the mantle peridotite (serpenitinized harzburgite) and dunite. (B) Pegmatitic gabbro within peridotite. (C) Isotropic pegmatitic gabbro and fine-grained mafic segregation.

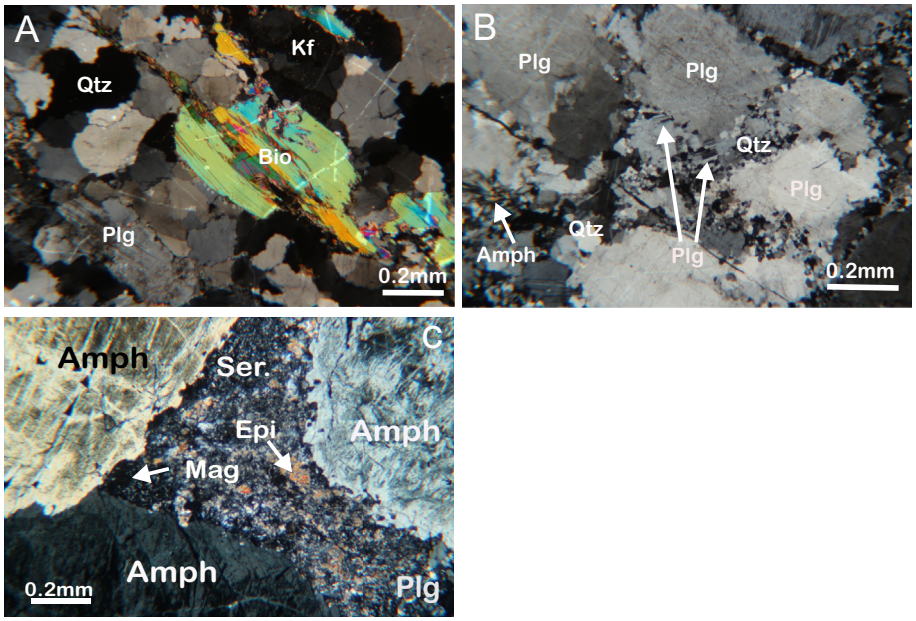

Fig. 4. Photomicrographs from the Mawat ophiolite, cross-polarized light: (A) Felsic dyke D1 with hybidiomorphic granular texture. (B) Felsic dyke D3 with coarse-grained porphyritic texture of plagioclase and quartz. (C) Coarse-grained amphibole and plagioclase in the pegmatitic gabbro. Plagioclase show weak twin lamellae and partially altered to sericite. Amph = amphibole; Bio = biotite; Epi = epidote; Mag = magnetite; Plg = plagioclase; Qtz = quartz, Kf = k-feldspar, and Ser = sericite.

layered amphibole-rich gabbros. Within the eastern thrust zone the pegmatitic and banded gabbros and peridotites occur. The contact relationships between the rock units are difficult to separate, because in most cases they are deformed and mixed with sediments and covered by soils. The area is also elevated with significant topographic relief hampering to reach the key outcrops.

In the eastern part of the ophiolite, late stage 3–30 m wide felsic intrusions of various compositions intrude the ultramafic rocks (serpentinized harzburgite and dunite; Fig. 2B). The Mawat ophiolite and the Gimo group rocks are metamorphosed in the greenschist facies (Jassim and Goff, 2006). The volcanic rocks in the Mawat ophiolite indicate an age of 105±5 Ma (K–Ar of hornblende; Aswad and Elias, 1988), and zircon U–Pb dating from the Daraban leucogranite in the central part of the Mawat ophiolite give an age of 96.8 ± 6.0 Ma (U–Pb zircon; Mohammad and Cornell, 2017).

The geochemical data of the mafic and ultramafic rocks show boninitic and MORB-like affinities (Al Humadi et al., 2018a). The arc-related chromitites (Ismail et al., 2010) indicate that the Mawat ophiolite formed in a supra-subduction zone setting resembling the other late Cretaceous Tethyan ophiolites along the Zagros Belt including the Oman ophiolite (Parlak et al., 2006; Dilek and Thy, 2009; Mohammad et al., 2014). The Pushtashan ophiolite, close to Mawat, shows similar tectonic setting

(Ismail et al., 2017). Therefore, in this article we consider Mawat as a supra-subduction zone ophiolite.

2.3. Samples

Four samples from two felsic dykes and a gabbro were collected from the eastern part of the Mawat ophiolite for U–Pb and Lu–Hf analysis (Fig. 2A). The felsic dyke D1 (includes two separate samples D1a and D1b from the same hand sample) has zirconium content of 19.7 ppm, the felsic dyke D3 34.3 ppm and the gabbro 64.3 ppm.

2.3.1. Felsic samples (D1a, D1b and D3)

The felsic dykes are NW-SE striking and intrude the ultramafic rocks of serpentinized harzburgite and dunite in the central and eastern part of the ophiolite. Dyke D1 is about 4 m and D3 about 30 m wide (Fig. 3A). The major minerals in granitic samples D1a and D1b include plagioclase, quartz, K-feldspar, tourmaline, muscovite and biotite and the accessories are apatite, ilmenite, magnetite, zircon, monazite and xenotime (Fig. 4A). The D1a and D1b are medium to coarse-grained with hypidiomorphic, granular, porphyritic and perthitic textures. Plagioclase is albite and K-feldspar is microcline. Both plagioclase and K-feldspar contain inclusions of quartz, biotite, muscovite, apatite and unknown minerals. The quartz grains are bimodal as large anhedral grains with undulatory extinction and as ribbons in and around plagioclase and K-feldspar grains. In some case the muscovite and plagioclase grains are slightly folded. The major minerals in tonalitic sample D3 include plagioclase, quartz, amphibole, and biotite with accessories, apatite, magnetite, K-feldspar, zircon, monazite and xenotime (Fig. 4B). The sample is medium to coarse-grained with hypidiomorphic granular, porphyritic textures. Plagioclase is albite and partially altered to sericite and epidote. Plagioclase, biotite and quartz grains show bimodal sizes. The undulatory extinction in quartz and the folding of muscovite are indications of later deformation. The field relationships show that the dykes sharply crosscut the host rock showing that they are younger.

2.3.2. Mafic sample (GB1)

The pegmatitic gabbro occurs as irregular small lenses within the ultramafic rocks in the eastern part of the ophiolite (Fig. 3B). Isotropic gabbro of irregular shape with mafic segregation also occurs (Fig. 3C). The rock is located within a thrust zone. It is composed of plagioclase, amphibole with accessory chlorite, ilmenite, rutile and magnetite (Fig. 4C). 1–2 mm sized plagioclase is the most common mineral with sub-ophitic texture. It shows weakly developed twin lamellae and is partially altered to sericite. Fine-grained plagioclase also occurs.

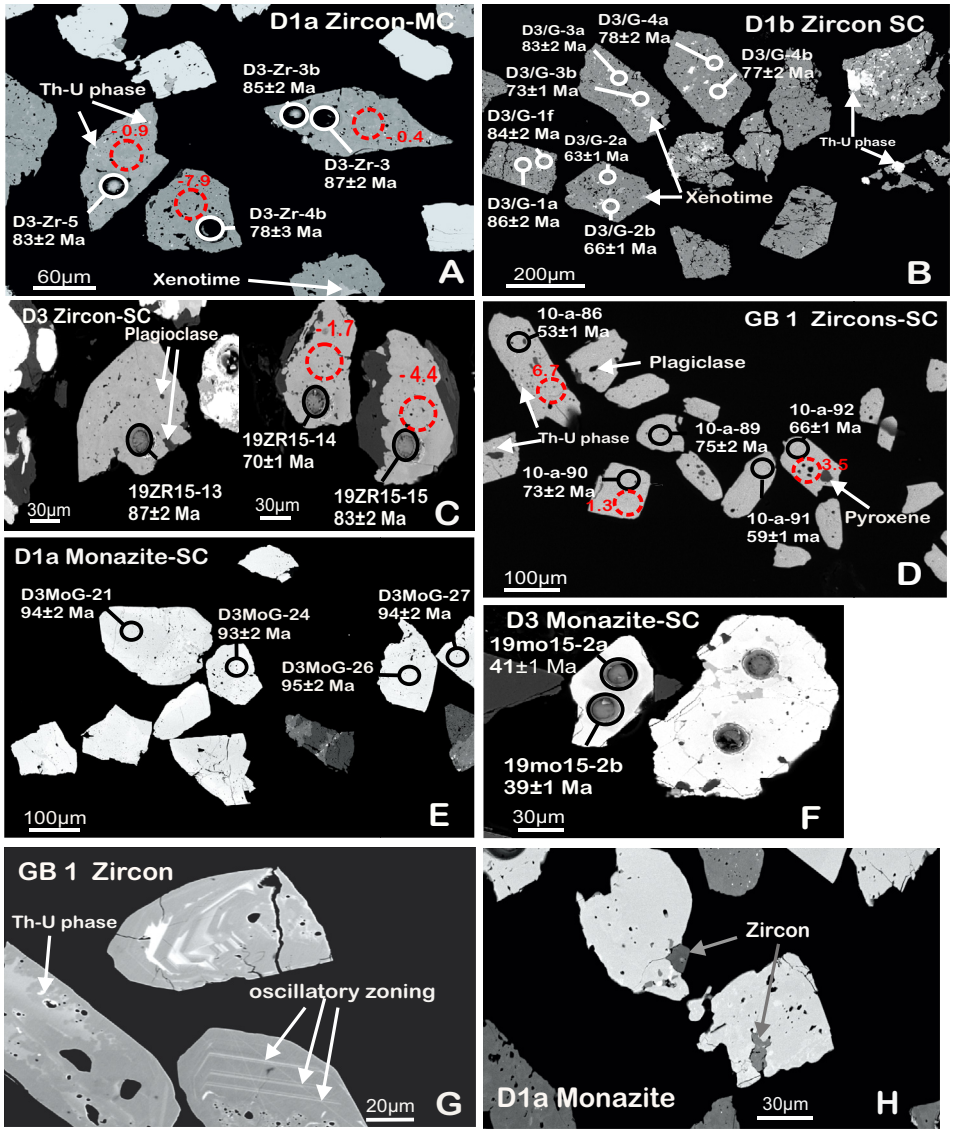

Fig. 5. Back Scattered Electron images of selected zircons and monazites from felsic dykes D1, D3 and gabbro GB1. Black and white solid circles represent U–Pb spots (25µm) with $^{206}Pb/^{238}U$ age; red dashed circles represent Lu–Hf spots (50µm) with initial ε_{Hf} (t) value. (A) Zircons from D1a. (B) Zircons from D1b. (C) Zircons from D3. (D) Zircons from the GB1. (E) Monazites from D1a. (F) Monazites from D3. (G) Zircons from GB1 showing the oscillatory zoning and Th–U phase. (H) Zircon inclusions in monazite.

Table 1
Data table of the Laser-Ablation Nu Plasma HR multicollector ICP-MS U–Pb zircon data for felsic sample D1a from the Mawat ophiolite. Location (N-35° 51. 24′) (E-45° 32. 55′).

Sample	Concentrations (ppm)			Ratios									Discordance	Ages (Ma)					
	Pb	Th	U	Th/U	$^{206}Pb/^{204}Pb$	$^{207}Pb/^{206}Pb$	1s	$^{207}Pb/^{235}U$	1s	$^{206}Pb/^{238}U$	1s	rho	% Concordance	$^{207}Pb/^{206}Pb$	1s	$^{207}Pb/^{235}U$	1s	$^{206}Pb/^{238}U$	1s
D3-Zr-3	40	n.a	3249	n.a	13803	0.0486	0.0007	0.0906	0.0021	0.0135	0.0003	0.81	-33	129	31	88	2	87	2
D3-Zr-3b	43	n.a	3532	n.a	8175	0.0475	0.0007	0.0867	0.0022	0.0132	0.0003	0.82	10.9	76	32	84	2	85	2
D3-Zr-4b	48	n.a	4507	n.a	1400	0.0482	0.0011	0.0810	0.0037	0.0122	0.0005	0.87	-29.8	111	49	79	3	78	3
D3-Zr-5	102	n.a	9174	n.a	36313	0.0483	0.0006	0.0857	0.0025	0.0129	0.0003	0.92	-26.8	112	25	84	2	83	2
D3-Zr-6	48	n.a	3444	n.a	26268	0.0479	0.0009	0.0943	0.0034	0.0143	0.0005	0.86	-1.5	93	42	91	3	91	3
D3-Zr-7	66	n.a	5225	n.a	9436	0.0473	0.0012	0.0837	0.0028	0.0128	0.0003	0.65	32.6	62	55	82	3	82	2
D3-Zr-8	34	n.a	2489	n.a	2330	0.0463	0.0013	0.0874	0.0033	0.0137	0.0003	0.63	627.5	12	58	85	3	88	2
D3-Zr-9	45	n.a	3570	n.a	2917	0.0446	0.0017	0.0774	0.0035	0.0126	0.0003	0.55	94.9	-41	77	76	3	81	2

Amphiboles (2–7 mm) are subhedral to euhedral.

3. Methods

3.1. U–Pb geochronology of zircon and monazite

Zircons and monazites were separated using the standard procedure with crushing, panning, heavy liquid separation, magnetic separation and hand picking. The analytical spots were selected on the basis of BSE-images conducted using a LEO 1530 Gemini scanning electron microscope at Åbo Akademi University Finland (felsic dyke D1a) and a JEOL JSM-7100F FE-SEM Schottky attached to an Oxford Instruments energy dispersive spectrometer (EDS) X-max (80 mm^2) in the Finnish Geosciences Research Laboratory at the Geological Survey of Finland in Espoo.

U–Pb analyses of felsic sample D1a were preformed using a Nu Plasma HR multicollector ICP-MS at the Geological Survey of Finland in Espoo using a technique very similar to Rosa et al. (2009) except that a Photon Machine Analyte G2 (for A2100) laser microprobe was used. In general, the analytical procedure followed that described in Huhma et al. (2012). The standards were the same as used with the Nu AttoM single collector ICPMS described below.

Zircon U–Pb dating of felsic (D1b and D3) and mafic (GB1**)** samples was performed using a Nu AttoM single collector ICPMS at Geological Survey of Finland, Espoo, using the similar procedure as described in Kara et al. (2018).

The calibration standard zircon GJ-1 (609 ± 1 Ma; Belousova et al., 2006), PL (337 ± 0.4 Ma; Sláma et al., 2007) and in-house standard A382 (1877 ± 2 Ma, Huhma et al., 2012) and the calibration standard monazite 44069 (424 ± 1 Ma; Aleinikoff et al., 2006) or in-house standard 117531 (272 ± 4 Ma) were run at the beginning and end of each analytical session, and at regular intervals during sessions. Raw data were corrected for the background, laser induced elemental fractionation, mass discrimination and drift in ion counter gains and reduced to U–Pb isotope ratios by calibration to concordant reference zircons, using the program Glitter (Van Achterbergh et al., 2001). Further data reduction including common lead correction and error propagation was performed using in-house excel spreadsheet. Errors include measured within-run errors (SD) and quadratic addition of reproducibility of standard (SE). To minimize the effects of laser-induced elemental fractionation, the depth-to-diameter ratio of the ablation pit was kept low, and isotopically homogeneous segments of the time-resolved traces were calibrated against the corresponding time interval for each mass in the reference zircon.

Plotting of the U–Pb isotopic data and age calculations were performed using the Isoplot/Ex 4.15 program (Ludwig, 2003).

3.2. Hf isotope analysis

The *in-situ* zircon Hf isotope analyses were performed using the same LA-ICP-MC-MS instrument as in method one described above. All analyses were made using the following parameters; beam diameter: 40–50 μm, pulse frequency: 5 Hz, beam energy density: 2.8 J/cm^2. Each ablation was preceded by a 30s on-mass background measurement. During the ablation the following masses were collected in static mode: ^{171}Yb, ^{172}Yb, ^{173}Yb, ^{175}Lu, $^{176}Hf–Yb–Lu$, ^{177}Hf, ^{178}Hf, ^{179}Hf. The total Hf signal obtained for zircons was typically 1.0–2.0 V. Isotopic ratios were measured using the Nu Plasma time-resolved analysis software. The isotopic ratios were later on calculated off-line using an Excel spreadsheet. The raw data were filtered at 2σ and corrected for mass discrimination using an exponential law. The mass discrimination factor for Hf was determined assuming $^{179}Hf/^{177}Hf = 0.7325$ (Patchett and Tatsumoto, 1981). The mass discrimination factor for Yb was determined assuming $^{173}Yb/^{171}Yb = 1.132685$ (Chu et al., 2002). The $^{176}Lu/^{175}Lu$ value of 0.02656 has also been used for the correction of the ^{176}Lu interference on ^{176}Hf (Scherer et al., 2000; Vervoort et al., 2004). A value

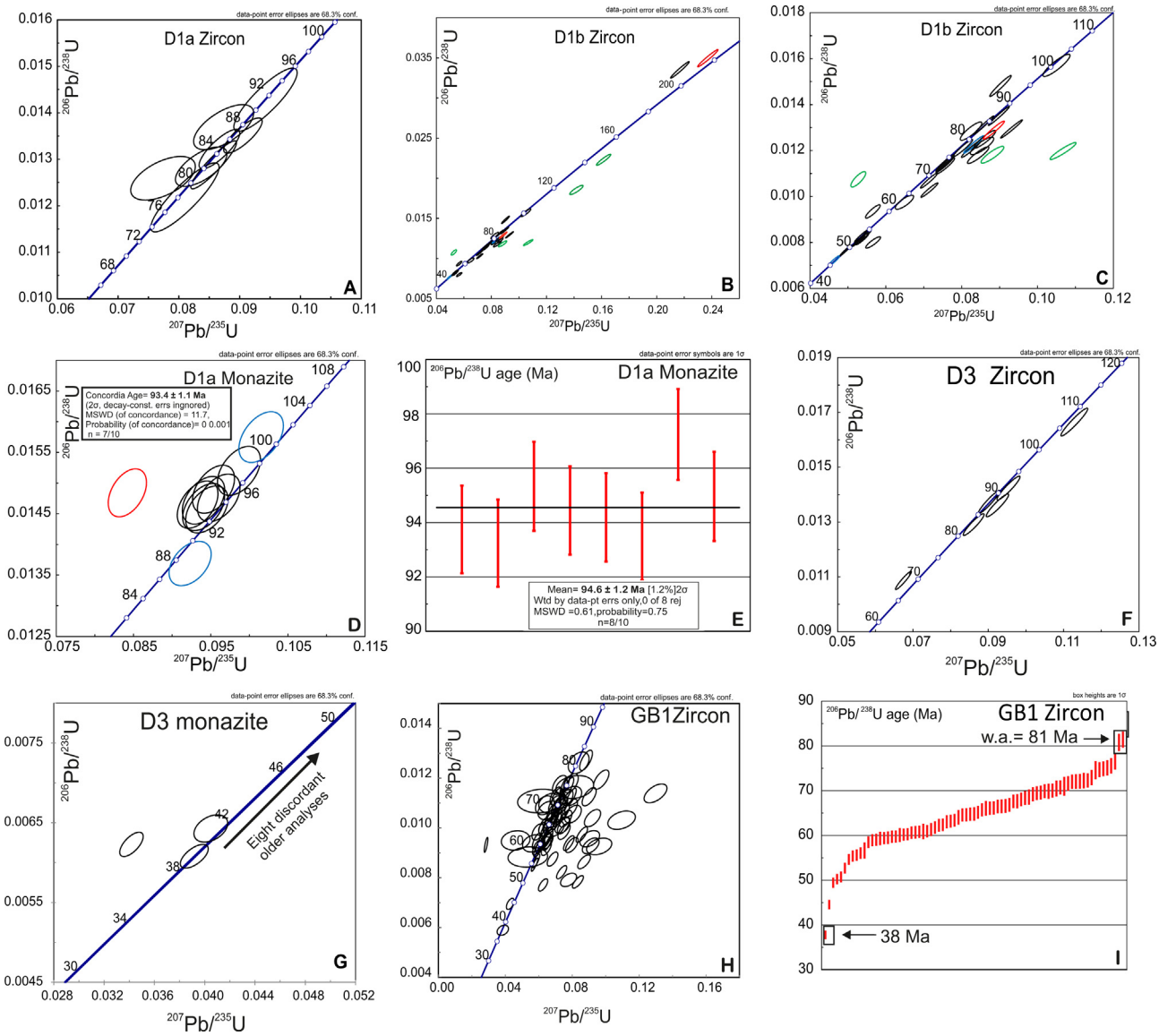

Fig. 6. U–Pb concordia and $^{206}Pb/^{238}U$ weighted average diagrams of zircons and monazites. (A) Age of zircons from felsic sample D1a using a Nu Plasma HR multicollector ICP-MS. (B and C) Age of zircons from felsic sample D1b using a Nu Plasma AttoM single collector ICP-MS. (D) Concordia age of monazites from D1a. Blue and red colours indicate analyses omitted from age calculation. (E) Weighted average $^{206}Pb/^{238}U$ age of monazites from sample D1a. (F) Age of zircons from D3. (G) Age of monazites from D3. (H) Age of zircons from GB1. (I) All the analyses of GB1 indicating the youngest and oldest ages (w. a. = weighted average). The blue, green and red colours in error ellipses refer to analyses which come from the same grain, respectively.

for the decay constant of ^{176}Lu of 1.867×10^{-11} a^{-1} has been used in all calculations (Scherer et al., 2000; Söderlund et al., 2004).

For the calculation of ε_{Hf} values we use present-day chondritic $^{176}Hf/^{177}Hf = 0.282785$ and $^{176}Lu/^{177}Hf = 0.0336$ (Bouvier et al., 2008). The zircon standard GJ-1 was run at frequent intervals for quality control. Multiple LA–MC–ICP–MS analyses, using the same instrumental parameters, of the reference zircon GJ-1 during the course of the present study yielded a $^{176}Hf/^{177}Hf$ of 0.28194 ± 6 (1σ, n = 35), which is just within error to results obtained by solution MC–ICP–MS analyses for GJ1 (0.281998 ± 7 Gerdes and Zeh, 2006; 0.282000 ± 5, Morel et al., 2008).

3.3. Whole-rock zirconium analysis

The zirconium (Zr) analysis was performed at Bureau Veritas Minerals, Vancouver, Canada, using ICP-MS method after lithium borate fusion.

4. Results

4.1. Samples D1a and D1b, felsic dyke

This dyke was analysed in two sessions from two separate samples from the same hand sample. The first session was performed using the MC instrument on the first mount (D1a). During the second session, more material from the sample was separated and placed on the second mount (D1b). These were analysed by the SC instrument.

4.1.1. Zircon

Twelve zircons were recovered from sample D1a. The zircons, 70–180 μm in size, are anhedral and broken prismatic grains with rough uneven surfaces. One elongated grain is 200 μm long. Some crystals might be just fragments of bigger crystals. The BSE-images show abundant dark and bright spots. The bright ones are inclusions identified as thorite and U–Th rich phases, and the less bright spots are xenotime and monazite and the dark spots are probably pores after fluid inclusions (Fig. 5A).

Table 2
Data table of the Laser-Ablation Nu Plasma AttoM single collector ICP-MS U–Pb zircon data for felsic sample D1b from the Mawat ophiolite. Location (N-35° 51. 24′) (E-45° 32.55′).

Sample	Concentrations (ppm)			Ratios									Disconrdance	Ages (Ma)					
	Pb	Th	U	Th/U	$^{206}Pb/^{204}Pb$	$^{207}Pb/^{206}Pb$	1s	$^{207}Pb/^{235}U$	1s	$^{206}Pb/^{238}U$	1s	rho	% Concordance	$^{207}Pb/^{206}Pb$	1s	$^{207}Pb/^{235}U$	1s	$^{206}Pb/^{238}U$	1s
D3/G- 1a	129.6	1049.5	8696	0.12	2377	0.0482	0.0002	0.0898	0.0018	0.0135	0.0003	0.98	22	110	9	87	2	86	2
D3/G-1 b	51.2	390	5547	0.07	1223	0.0468	0.0002	0.0534	0.0011	0.0083	0.0002	0.98	10	41	10	53	1	53	1
D3/G-1c	103.5	1856.7	11299	0.16	1078	0.0475	0.0002	0.0529	0.0011	0.0081	0.0002	0.98	8	74	9	52	1	52	1
D3/G-1d	99	1373.4	11464	0.12	1036	0.0469	0.0002	0.0495	0.0010	0.0077	0.0002	0.98	8	42	9	49	1	49	1
D3/G-1e	44	1263.0	4654	0.27	946	0.0478	0.0002	0.0544	0.0011	0.0083	0.0002	0.98	8	88	10	54	1	53	1
D3/G-1f	366	8732.4	25114	0.35	1298	0.0475	0.0002	0.0859	0.0017	0.0131	0.0003	0.99	15	75	8	84	2	84	2
D3/G-2a	28	163.7	2778	0.06	210848	0.0483	0.0007	0.0649	0.0016	0.0097	0.0002	0.80	53	114	34	64	2	63	1
D3/G-2b	26	102.0	2450	0.04	198228	0.0505	0.0003	0.0715	0.0015	0.0103	0.0002	0.97	30	216	12	70	1	66	1
D3/G-2c	29	219.8	2594	0.08	217159	0.0484	0.0003	0.0714	0.0015	0.0107	0.0002	0.97	55	120	13	70	1	69	1
D3/G-2d	48	148.5	4231	0.04	368500	0.0485	0.0004	0.0757	0.0016	0.0113	0.0002	0.94	58	122	17	74	2	73	1
D3/G-3a	118	4863.8	6333	0.77	195	0.0522	0.0002	0.0931	0.0019	0.0129	0.0003	0.98	4	295	8	90	2	83	2
D3/G-3b	46	925.2	3901	0.24	2248	0.0478	0.0003	0.0756	0.0016	0.0115	0.0002	0.97	19	92	13	74	1	73	1
D3/G-4a	52	604.7	4233	0.14	385841	0.0481	0.0003	0.0804	0.0017	0.0121	0.0002	0.96	72	106	14	78	2	78	2
D3/G-4b	34	450.9	2732	0.17	250250	0.0496	0.0003	0.0825	0.0017	0.0121	0.0002	0.97	43	176	13	81	2	77	2
D3/G-5a	24	173.1	2061	0.08	179390	0.0481	0.0003	0.0756	0.0016	0.0114	0.0002	0.96	68	104	14	74	1	73	1
D3/G-5b	30	286.5	2362	0.12	3552	0.0466	0.0005	0.0825	0.0019	0.0128	0.0003	0.87	36	28	27	80	2	82	2
D3/G-6a	46	179.8	3667	0.05	5903	0.0492	0.0002	0.0832	0.0017	0.0123	0.0002	0.97	29	157	11	81	2	79	2
D3/G-6b	27	216	3588	0.06	3264	0.0467	0.0003	0.0464	0.0010	0.0072	0.0001	0.95	19	34	16	46	0.9	46	0.9
D3/G-7a	17	563	744	0.76	123511	0.0525	0.0004	0.1615	0.0034	0.0223	0.0005	0.94	45	309	16	152	3.0	142	2.8
D3/G-7b	7	81	476	0.17	311	0.0646	0.0005	0.1067	0.0023	0.0120	0.0002	0.94	4	762	15	103	2.1	77	1.5
D3/G-7c	16	397	852	0.47	115550	0.0555	0.0006	0.1417	0.0032	0.0185	0.0004	0.88	27	431	24	135	2.8	118	2.4
D3/G-7d	10	95	830	0.11	71916	0.0541	0.0006	0.0881	0.0020	0.0118	0.0002	0.88	20	375	24	86	1.9	76	1.5
D3/G-7e	13	47	1222	0.04	1045	0.0356	0.0005	0.0527	0.0013	0.0107	0.0002	0.81	37	-662	39	52	1.2	69	1.4
D3/G-8a	34	280	2873	0.10	253672	0.0500	0.0004	0.0861	0.0019	0.0125	0.0003	0.91	40	196	21	84	1.8	80	1.6
D3/G-8b	37	355	3216	0.11	277288	0.05076	0.0007	0.0854	0.0020	0.0122	0.0002	0.83	34	230	30	83	1.91	78	1.6
D3/G-9a	52	30496	1220	24.99	204	0.04419	0.0002	0.0902	0.0019	0.0148	0.0003	0.97	5	-100	13	88	1.74	95	1.9
D3/G-9b	13	970	1104	0.878	1389	0.05185	0.0005	0.0844	0.0019	0.0118	0.0002	0.90	11	279	22	82	1.74	76	1.5
D3/G-0a	100	576	2634	0.219	776	0.04920	0.0002	0.2372	0.0049	0.0350	0.0007	0.98	26	157	11	216	3.99	222	4.4
D3/G-0b	33	54	2751	0.019	253373	0.04979	0.0003	0.0885	0.0018	0.0129	0.0003	0.96	44	185	13	86	1.72	83	1.7
D3/G-11	25	117	1658	0.070	191082	0.04848	0.0005	0.1050	0.0024	0.0157	0.0003	0.89	79	123	24	101	2.16	100	2.0
D3/G-12	188	2490	5690	0.438	3089	0.04695	0.0002	0.2168	0.0045	0.0335	0.0007	0.98	78	46	11	199	3.71	212	4.2
D3/G-13	25	167	2805	0.06	1526	0.0439	0.0005	0.0566	0.0013	0.0093	0.0002	0.88	17	-116	26	56	1.2	60	1.2
D3/G-14a	19	326	2526	0.13	139000	0.0514	0.0006	0.0567	0.0013	0.0080	0.0002	0.88	20	258	25	56	1.2	51	1.0
D3/G-14b	23	418	2983	0.14	3329	0.0479	0.0004	0.0538	0.0012	0.0081	0.0002	0.93	18	93	18	53	1.1	52	1.1
[a]Average of Th/U values.				[a]0.16															

[a] Average of Th/U values.

Table 3
Data table of the Laser-Ablation Nu Plasma AttoM single collector ICP-MS U–Pb monazite data for felsic sample D1a from the Mawat ophiolite. Location (N-35° 51. 24′) (E-45° 32. 55′).

Sample	Concentrations (ppm)			Ratios									Disconrdance	Ages (Ma)					
	Pb	Th	U	Th/U	$^{206}Pb/^{204}Pb$	$^{207}Pb/^{206}Pb$	1s	$^{207}Pb/^{235}U$	1s	$^{206}Pb/^{238}U$	1s	rho	% Concordance	$^{207}Pb/^{206}Pb$	1s	$^{207}Pb/^{235}U$	1s	$^{206}Pb/^{238}U$	1s
D3MoG-21	888	145101	4308	34	243917	0.0462	0.0014	0.0933	0.0017	0.0146	0.0003	0.46	838	8	72	91	2	94	2
D3MoG-24	1189	204199	4847	42	268828	0.0470	0.0015	0.0945	0.0018	0.0146	0.0003	0.44	172	52	72	92	2	93	2
D3MoG-26	909	149196	4181	36	237282	0.0464	0.0014	0.0954	0.0018	0.0149	0.0003	0.45	413	20	72	92	2	95	2
D3MoG-27	758	123056	3717	33	207670	0.0472	0.0015	0.0960	0.0018	0.0148	0.0003	0.45	150	59	72	93	2	94	2
D3MoG-28a	637	101754	3664	28	202136	0.0464	0.0014	0.0941	0.0018	0.0147	0.0003	0.43	471	16	73	91	2	94	2
D3MoG-28b	622	101001	3489	29	190569	0.0467	0.0014	0.0941	0.0018	0.0146	0.0003	0.44	243	35	72	91	2	93	2
D3MoG-29a	1274	217923	4492	49	254390	0.0471	0.0014	0.0987	0.0018	0.0152	0.0003	0.45	173	53	72	96	2	97	2
D3MoG-29b	1303	222640	4264	52	248566	0.0468	0.0014	0.1015	0.0019	0.0157	0.0003	0.45	251	37	72	98	2	101	2
D3MoG-30	627	111398	3388	33	172158	0.0489	0.0015	0.0923	0.0018	0.0137	0.0002	0.42	59	144	72	90	2	88	2
D3MoG-31	822	143290	4327	33	2320	0.0412	0.0013	0.0842	0.0016	0.0148	0.0003	0.43	124	-278	77	82	2	95	2

Table 4
Data table of the Laser-Ablation Nu Plasma AttoM single collector ICP-MS U–Pb zircon data for felsic sample D3 from Mawat ophiolite. Location (N-35° 50 41′) (E-45° 33 12′).

Sample	Concentrations (ppm)			Ratios									Disconrdance	Ages (Ma)					
	Pb	Th	U	Th/U	$^{206}Pb/^{204}Pb$	$^{207}Pb/^{206}Pb$	1s	$^{207}Pb/^{235}U$	1s	$^{206}Pb/^{238}U$	1s	rho	% Concordance	$^{207}Pb/^{206}Pb$	1s	$^{207}Pb/^{235}U$	1s	$^{206}Pb/^{238}U$	1s
19ZR-3b	142	695	6832	0.10	282	0.0492	0.0003	0.1129	0.0024	0.0166	0.0003	0.95	7	156	15	109	2	106	2
19ZR-7	79	623	5442	0.11	288509	0.0486	0.0004	0.0954	0.0020	0.0142	0.0003	0.94	70	128	17	92	2	91	2
19ZR15-9	457	18811	29211	0.64	5097	0.0476	0.0003	0.0902	0.0019	0.0137	0.0003	0.95	40	82	15	88	2	88	2
19ZR15-13	33	58	2445	0.02	143074	0.0493	0.0004	0.0924	0.0020	0.0136	0.0003	0.93	53	161	18	90	2	87	2
19ZR15-14	67	328	5788	0.06	1038	0.0450	0.0003	0.0675	0.0014	0.0109	0.0002	0.95	12	-55	16	66	1	70	1
19ZR15-15	34	62	2610	0.02	144526	0.0484	0.0004	0.0861	0.0018	0.0129	0.0003	0.93	67	118	18	84	2	83	2
Average of Th/U values				[a]0.16															

[a] Average of Th/U values.

Table 5
Data table of the Laser-Ablation Nu Plasma AttoM single collector ICP-MS U–Pb monazite data for felsic sample D3 from the Mawat ophiolite. Location (N-35° 50 41′) (E-45° 33 12′).

Sample	Concentrations (ppm)			Ratios								Discordance	Ages (Ma)					
	Pb	Th	U	Th/U	$^{206}Pb/^{204}Pb$	$^{207}Pb/^{206}Pb$	1s	$^{207}Pb/^{235}U$	1s	$^{206}Pb/^{238}U$	1s	rho	% Concordance	$^{207}Pb/^{206}Pb$	1s	$^{207}Pb/^{235}U$	1s	$^{206}Pb/^{238}U$	1s
19mo15-1	180	20612	7155	3	699	0.0398	0.0012	0.0342	0.0006	0.0062	0.0001	0.65	6	-364	79	34	1	40	1
19mo15-2a	90	21286	1711	12	48857	0.0457	0.0015	0.0405	0.0009	0.0064	0.0001	0.38	-1421	-19	78	40	1	41	1
19mo15-2b	81	11801	3231	4	87079	0.0467	0.0015	0.0392	0.0007	0.0061	0.0001	0.62	88	36	74	39	1	39	1
19mo15-3a	245	46955	216	217	29	0.2183	0.0067	0.8701	0.0150	0.0289	0.0005	0.66	6	2968	49	636	8	184	3
19mo15-3b	297	42543	405	105	36	0.1813	0.0055	0.7098	0.0121	0.0284	0.0005	0.68	6	2665	50	545	7	180	3
19mo15-4a	72	16393	28	583	37	0.0723	0.0026	0.2667	0.0063	0.0267	0.0005	0.39	6	995	72	240	5	170	3
19mo15-4b	119	27067	47	577	45	0.1070	0.0037	0.3412	0.0077	0.0231	0.0004	0.44	5	1749	63	298	6	147	3
19mo15-4c	105	26168	46	564	43	0.1044	0.0037	0.3186	0.0072	0.0221	0.0004	0.43	5	1704	63	281	6	141	3
19mo15-5a	180	37683	116	325	122	0.2229	0.0081	0.6241	0.0150	0.0203	0.0004	0.41	4	3002	57	492	9	130	2
19mo15-5b	252	49811	232	214	61	0.1035	0.0033	0.2755	0.0051	0.0193	0.0003	0.60	4	1688	57	247	4	123	2
19mo15-6	126	27302	55	493	3628	0.2200	0.0092	0.4715	0.0146	0.0155	0.0003	0.30	3	2981	66	392	10	99	2

During the first session (MC), eight grains from sample D1a were analysed. The analyses plot on or close to the concordia curve but form only a very loose cluster with single concordia and $^{206}Pb/^{238}U$ ages ranging from 91 to 78 Ma (Table 1; Fig. 6A).

Sample D1b was analysed during the second session (SC) and 14 zircon grains were analysed placing as many spots as possible on the grains (n = 34). The BSE-images show that the anhedral, fragmental or shapeless grains are 80–220 μm in size. Their spongy domains contain bright and grey inclusions. The bright ones are thorite and the grey ones are xenotime. The black spots are pores (Fig. 5B).

On the concordia diagram the data form a range of concordant, near-concordant, discordant and reversely discordant ages (Figs. 6B and 6C) whose $^{206}Pb/^{238}U$ ages range from 222 Ma to 46 Ma (Table 2). The concordia and $^{206}Pb/^{238}U$ ages are in quite good accordance.

4.1.2. Monazite

Thirteen monazite grains were recovered from sample D1a. The crystals range from 70-300 μm in length, with anhedral to subhedral shapes (Fig. 5E). The BSE-images show xenotime, thorite and zircon inclusions (Fig. 5H). Ten spots from ten grains were analysed with SC. Seven analyses form a cluster which yields a concordia age of 93.4 ± 1.1 Ma (Fig. 6D; 2σ; MSWD = 11.7). One concordant analysis is younger with a $^{206}Pb/^{238}U$ age of 88 ± 2 Ma and one concordant analysis is older with a $^{206}Pb/^{238}U$ age of 101 ± 2 Ma (Table 3). The remaining analysis is reversely discordant. Omitting the oldest and youngest analyses, eight $^{206}Pb/^{238}U$ analyses give a weighted average age of 94.6 ± 1.2 Ma (Fig. 6E; 2σ, MSWD = 0.61; hereafter referred to as ~ 95 Ma) which we consider the best estimate for the crystallisation age of the monazite.

4.2. Sample D3, felsic dyke

4.2.1. Zircon

The zircon grains are 80–100 μm in length, broken into shapeless fragments. The BSE-images display dark inclusions and patches of mineral xenotime and an unknown Si, Ca, Al, K, and Fe bearing phase (Fig. 5C). Six analyses yielded $^{206}Pb/^{238}U$ ages of from 106 Ma (high common Pb) to 70 Ma (reversely discordant). The oldest of the remaining four grains is 91 Ma (Fig. 6F; Table 4).

4.2.2. Monazite

Most monazite grains are irregularly shaped, just a few are subhedral, and their size ranges from 70 to 150 μm. The BSE-images show dark and bright spots (Fig. 5F). Eleven spots on six grains were analysed with SC. Three grains plot on or near the concordia and yield $^{206}Pb/^{238}U$ ages of 41 Ma, 40 Ma (reversely discordant) and 39 Ma. The remaining eight analyses are older and discordant and not considered further (Fig. 6G; Table 5).

4.3. Sample GB1, gabbro

The zircons consist of subhedral or shapeless (or broken) grains but euhedral grains, 50–200 μm in length, also exist. A few show a weak internal zoning (Fig. 5G). The BSE-images show that the grains contain black spots of plagioclase and pyroxene inclusions and white spots of Th- and U-rich phase (Fig. 5D). 87 grains and 89 spots were analysed with SC of which 11 analyses were of low quality/very discordant and were rejected. The remaining 78 analyses plot on/close to the concordia curve or are discordant or reversely discordant (Fig. 6H). They form a semi-continuous declining range of $^{206}Pb/^{238}U$ ages from 81 Ma to 38 Ma (Table 6). The oldest two grains give a weighted average $^{206}Pb/^{238}U$ age of 81.2 ± 2.5 Ma (2σ, MSWD = 0.063; Fig. 6I; hereafter referred to as 81 Ma).

4.4. Hf isotope analysis

Nine Hf isotope determinations were performed on nine zircons from

Table 6
Data table of the Laser-Ablation Nu Plasma AttoM single collector ICP-MS U–Pb zircon data for gabbro sample GB1 from the Mawat ophiolite. Location (N-35° 52 24′) (E-45° 33 11′).

Sample	Concentrations (ppm)			Ratios									Disconrdance	Ages (Ma)					
	Pb	Th	U	Th/U	$^{206}Pb/^{204}Pb$	$^{207}Pb/^{206}Pb$	1s	$^{207}Pb/^{235}U$	1s	$^{206}Pb/^{238}U$	1s	rho	% Concordance	$^{207}Pb/^{206}Pb$	1s	$^{207}Pb/^{235}U$	1s	$^{206}Pb/^{238}U$	1s
MOC-Gab-10-a-1a	0	0	50	0.01	2401	0.0439	0.0032	0.0567	0.0043	0.0094	0.0002	0.23	31	-117	172	56	4	60	1
10-a-1b	5	268	419	0.64	22386	0.0480	0.0008	0.0698	0.0018	0.0106	0.0002	0.75	52	97	41	68	2	68	1
10-a-2	3	436	137	3.18	7229	0.0643	0.0019	0.0921	0.0032	0.0104	0.0002	0.55	8	751	60	89	3	67	1
10-a-3	15	1578	1229	1.28	53018	0.0490	0.0005	0.0576	0.0013	0.0085	0.0002	0.87	34	146	26	57	1	55	1
10-a-4	6	910	474	1.92	18869	0.0772	0.0013	0.0834	0.0022	0.0078	0.0002	0.76	4	1127	34	81	2	50	1
10-a-5	4	308	262	1.18	12886	0.0489	0.0012	0.0655	0.0020	0.0097	0.0002	0.64	32	142	55	64	2	62	1
10-a-6a	4	103	305	0.34	219	0.0222	0.0003	0.0285	0.0007	0.0093	0.0002	0.78	4	[c]n.c	[c]n.c	29	1	60	1
10-a-6b	1	42	61	0.70	3308	0.0447	0.0028	0.0660	0.0043	0.0107	0.0003	0.28	44	-71	147	65	4	69	2
10-a-7	6	435	416	1.05	20794	0.0466	0.0009	0.0636	0.0017	0.0099	0.0002	0.73	96	30	45	63	2	63	1
[b]~~10-a-10a~~	~~1~~	~~29~~	~~55~~	~~0.53~~	~~46~~	~~0.0943~~	~~0.0022~~	~~0.1227~~	~~0.0035~~	~~0.0094~~	~~0.0002~~	~~0.62~~	~~3~~	~~#NUM!~~	~~#NUM!~~	~~133~~	~~4~~	~~61~~	~~1~~
[b]~~10-a-10b~~	~~1~~	~~2~~	~~2~~	~~0.70~~	~~886~~	~~0.8023~~	~~0.0263~~	~~8.9686~~	~~0.2746~~	~~0.0811~~	~~0.0026~~	~~0.46~~	~~10~~	~~4926~~	~~46~~	~~2335~~	~~28~~	~~503~~	~~16~~
10-a-10c	2	185	140	1.32	7494	0.0553	0.0020	0.0805	0.0033	0.0106	0.0002	0.45	14	424	80	79	3	68	1
[b]~~10-a-10d~~	~~3~~	~~18~~	~~60~~	~~0.30~~	~~26~~	~~0.2808~~	~~0.0046~~	~~0.4483~~	~~0.0107~~	~~0.0116~~	~~0.0003~~	~~0.76~~	~~3~~	~~3368~~	~~25~~	~~376~~	~~7~~	~~74~~	~~2~~
10-a-11	7	788	372	2.12	20277	0.0470	0.0009	0.0704	0.0019	0.0109	0.0002	0.72	80	51	44	69	2	70	1
10-a-12	1	159	72	2.23	3937	0.0423	0.0024	0.0637	0.0037	0.0109	0.0002	0.31	2464	-207	134	63	4	70	2
10-a-13	3	260	192	1.36	10000	0.0532	0.0014	0.0761	0.0025	0.0104	0.0002	0.60	17	337	58	74	2	67	1
10-a-14	5	649	305	2.13	14189	0.0477	0.0011	0.0609	0.0018	0.0093	0.0002	0.65	44	83	53	60	2	59	1
10-a-15	11	1612	643	2.51	30571	0.0493	0.0007	0.0645	0.0016	0.0095	0.0002	0.80	33	164	34	63	2	61	1
10-a-16	1	70	125	0.56	4978	0.0713	0.0026	0.0778	0.0032	0.0079	0.0002	0.46	5	967	73	76	3	51	1
10-a-17	3	281	195	1.44	10543	0.0532	0.0014	0.0792	0.0026	0.0108	0.0002	0.60	18	338	58	77	2	69	1
[b]~~10-a-18~~	~~91~~	~~764~~	~~513~~	~~1.49~~	~~21~~	~~0.5117~~	~~0.0033~~	~~2.2971~~	~~0.0484~~	~~0.0326~~	~~0.0007~~	~~0.95~~	~~7~~	~~4275~~	~~9~~	~~1211~~	~~15~~	~~207~~	~~4~~
10-a-19	5	449	313	1.44	15773	0.0452	0.0010	0.0629	0.0019	0.0101	0.0002	0.66	921	-43	54	62	2	65	1
10-a-20	7	469	452	1.04	25408	0.0512	0.0008	0.0793	0.0020	0.0112	0.0002	0.78	26	249	37	78	2	72	1
10-a-21	9	512	899	0.57	39139	0.0488	0.0007	0.0584	0.0014	0.0087	0.0002	0.82	35	140	33	58	1	56	1
10-a-22	5	525	353	1.49	16583	0.0602	0.0011	0.0780	0.0021	0.0094	0.0002	0.73	9	612	39	76	2	60	1
10-a-24	0	0	31	0.01	1473	0.0353	0.0043	0.0462	0.0057	0.0095	0.0003	0.13	-190	-688	309	46	5	61	2
10-a-25	1	70	119	0.59	3505	0.0474	0.0026	0.0385	0.0022	0.0059	0.0001	0.31	14	70	127	38	2	38	1
10-a-26	0	0	23	0.01	1013	0.0439	0.0064	0.0535	0.0078	0.0088	0.0003	0.09	11	-117	327	53	8	57	2
10-a-27	4	766	295	2.59	10214	0.0448	0.0013	0.0429	0.0015	0.0069	0.0001	0.55	366	-65	71	43	1	45	1
10-a-28	1	11	132	0.08	6085	0.0711	0.0022	0.0911	0.0033	0.0093	0.0002	0.52	6	961	63	88	3	60	1
10-a-29	3	219	182	1.20	9668	0.0507	0.0014	0.0745	0.0025	0.0107	0.0002	0.57	23	225	63	73	2	68	1
10-a-30	2	52	165	0.31	8107	0.0439	0.0015	0.0595	0.0024	0.0098	0.0002	0.48	-348	-118	84	59	2	63	1
10-a-31	2	105	189	0.56	8894	0.0499	0.0014	0.0652	0.0023	0.0095	0.0002	0.56	23	193	66	64	2	61	1
10-a-32	5	441	356	1.24	17031	0.0494	0.0010	0.0656	0.0019	0.0096	0.0002	0.70	30	166	47	65	2	62	1
10-a-33	4	387	326	1.19	15376	0.0491	0.0011	0.0644	0.0019	0.0095	0.0002	0.67	31	154	50	63	2	61	1
10-a-34	5	1051	338	3.11	12918	0.0589	0.0013	0.0626	0.0018	0.0077	0.0002	0.67	8	562	47	62	2	50	1
10-a-35	2	2	175	0.01	8564	0.0553	0.0014	0.0751	0.0024	0.0099	0.0002	0.61	13	423	56	74	2	63	1
10-a-36	4	445	225	1.98	11253	0.0537	0.0013	0.0747	0.0024	0.0101	0.0002	0.62	16	360	55	73	2	65	1
10-a-37	2	24	114	0.21	7075	0.0482	0.0022	0.0838	0.0041	0.0126	0.0003	0.37	39	109	104	82	4	81	2
10-a-38	1	27	56	0.48	2770	0.0490	0.0035	0.0675	0.0050	0.0100	0.0002	0.24	17	146	161	66	5	64	2
10-a-39	5	411	355	1.16	18638	0.0462	0.0009	0.0676	0.0019	0.0106	0.0002	0.71	143	7	47	66	2	68	1
10-a-40	0	6	34	0.18	1988	0.0508	0.0046	0.0815	0.0075	0.0116	0.0003	0.18	14	231	197	80	7	75	2
10-a-41	2	199	160	1.24	8923	0.0451	0.0011	0.0701	0.0022	0.0113	0.0002	0.62	205	-52	60	69	2	72	2
10-a-43	1	2	57	0.04	2888	0.0771	0.0036	0.1095	0.0054	0.0103	0.0002	0.35	5	1123	91	106	5	66	2
10-a-44	7	1083	347	3.12	18534	0.0487	0.0008	0.0728	0.0019	0.0108	0.0002	0.76	40	135	40	71	2	69	1

(*continued on next page*)

Table 6 (*continued*)

Sample	Concentrations (ppm)			Ratios									Disconrdance	Ages (Ma)					
	Pb	Th	U	Th/U	$^{206}Pb/^{204}Pb$	$^{207}Pb/^{206}Pb$	1s	$^{207}Pb/^{235}U$	1s	$^{206}Pb/^{238}U$	1s	rho	% Concordance	$^{207}Pb/^{206}Pb$	1s	$^{207}Pb/^{235}U$	1s	$^{206}Pb/^{238}U$	1s
10-a-46a	3	154	222	0.70	10182	0.0621	0.0015	0.0798	0.0025	0.0093	0.0002	0.63	8	679	51	78	2	60	1
10-a-47	4	235	254	0.93	15904	0.0503	0.0011	0.0883	0.0025	0.0127	0.0003	0.69	32	211	48	86	2	81	2
10-a-48	6	297	418	0.71	22719	0.0477	0.0009	0.0726	0.0020	0.0110	0.0002	0.74	61	85	42	71	2	71	1
10-a-49	1	80	76	1.05	4240	0.0510	0.0025	0.0793	0.0042	0.0113	0.0003	0.35	19	241	110	78	4	72	2
10-a-50	5	372	283	1.31	15193	0.0492	0.0011	0.0741	0.0022	0.0109	0.0002	0.67	34	159	51	73	2	70	1
10-a-51	2	165	152	1.08	7565	0.0478	0.0018	0.0666	0.0028	0.0101	0.0002	0.46	35	90	87	65	3	65	1
10-a-52	5	80	439	0.18	25158	0.0484	0.0008	0.0778	0.0020	0.0117	0.0002	0.76	51	119	40	76	2	75	2
10-a-53	9	89	971	0.09	44711	0.0508	0.0006	0.0658	0.0016	0.0094	0.0002	0.85	25	230	28	65	1	60	1
10-a-54	6	721	367	1.97	18252	0.0480	0.0010	0.0674	0.0019	0.0102	0.0002	0.69	46	101	48	66	2	65	1
10-a-55	4	375	208	1.81	11132	0.0461	0.0013	0.0694	0.0024	0.0109	0.0002	0.57	103	0	66	68	2	70	1
10-a-56	2	100	126	0.79	6250	0.0532	0.0019	0.0742	0.0030	0.0101	0.0002	0.46	15	339	80	73	3	65	1
10-a-57	3	138	171	0.81	9932	0.0487	0.0015	0.0792	0.0029	0.0118	0.0003	0.52	37	132	72	77	3	76	2
[b]~~10-a-58~~	~~5~~	~~264~~	~~451~~	~~0.59~~	~~20514~~	~~0.0593~~	~~0.0010~~	~~0.0761~~	~~0.0020~~	~~0.0093~~	~~0.0002~~	~~0.76~~	~~10~~	~~576~~	~~37~~	~~74~~	~~2~~	~~60~~	~~1~~
10-a-59	3	271	270	1.00	11533	0.0566	0.0014	0.0683	0.0021	0.0087	0.0002	0.63	11	476	53	67	2	56	1
10-a-65	1	79	103	0.77	4805	0.0686	0.0027	0.0905	0.0039	0.0096	0.0002	0.43	6	887	79	88	4	61	1
10-a-67	10	496	818	0.61	40899	0.0501	0.0007	0.0709	0.0017	0.0103	0.0002	0.84	30	201	30	70	2	66	1
10-a-70	2	43	187	0.23	9541	0.0471	0.0015	0.0677	0.0025	0.0104	0.0002	0.53	52	53	72	67	2	67	1
[b]~~10-a-71~~	~~4~~	~~84~~	~~234~~	~~0.36~~	~~12862~~	~~0.1295~~	~~0.0019~~	~~0.2009~~	~~0.0050~~	~~0.0113~~	~~0.0002~~	~~0.80~~	~~3~~	~~2091~~	~~26~~	~~186~~	~~4~~	~~72~~	~~2~~
[b]~~10-a-74~~	~~10~~	~~28~~	~~671~~	~~0.04~~	~~105~~	~~0.0201~~	~~0.0002~~	~~0.0273~~	~~0.0006~~	~~0.0098~~	~~0.0002~~	~~0.91~~	~~3~~	~~#NUM!~~	~~#NUM!~~	~~27~~	~~1~~	~~63~~	~~1~~
10-a-76	1	59	65	0.90	2925	0.0753	0.0037	0.0961	0.0050	0.0093	0.0002	0.34	5	1077	96	93	5	59	1
10-a-77	3	28	276	0.10	15086	0.0458	0.0011	0.0710	0.0022	0.0112	0.0002	0.65	195	-14	55	70	2	72	2
[b]~~10-a-78~~	~~0~~	~~1~~	~~3~~	~~0.25~~	~~93~~	~~0.0354~~	~~0.0167~~	~~0.0239~~	~~0.0108~~	~~0.0049~~	~~0.0007~~	~~0.01~~	~~1~~	~~-678~~	~~969~~	~~24~~	~~11~~	~~31~~	~~4~~
10-a-80	1	124	48	2.59	2574	0.0448	0.0034	0.0680	0.0053	0.0110	0.0003	0.23	32	-66	175	67	5	71	2
10-a-81	5	468	378	1.24	15127	0.0650	0.0012	0.0737	0.0020	0.0082	0.0002	0.72	7	775	39	72	2	53	1
10-a-82	2	9	157	0.05	8506	0.0495	0.0016	0.0762	0.0028	0.0112	0.0002	0.52	29	170	73	75	3	72	2
10-a-83	2	10	205	0.05	11186	0.0581	0.0014	0.0901	0.0028	0.0113	0.0002	0.63	12	534	52	88	3	72	2
10-a-84	6	422	399	1.06	18783	0.0639	0.0011	0.0857	0.0023	0.0097	0.0002	0.75	8	738	36	84	2	62	1
[b]~~10-a-86~~	~~4~~	~~172~~	~~379~~	~~0.45~~	~~238~~	~~0.0038~~	~~0.0001~~	~~0.0043~~	~~0.0001~~	~~0.0082~~	~~0.0002~~	~~0.72~~	~~8~~	~~#NUM!~~	~~#NUM!~~	~~4~~	~~0~~	~~53~~	~~1~~
10-a-89	7	137	610	0.22	34482	0.0468	0.0007	0.0755	0.0019	0.0117	0.0002	0.80	121	40	35	74	2	75	2
10-a-90	2	51	107	0.48	5915	0.0827	0.0024	0.1298	0.0045	0.0114	0.0003	0.55	6	1262	56	124	4	73	2
10-a-91	4	324	370	0.88	16459	0.0464	0.0010	0.0589	0.0018	0.0092	0.0002	0.66	91	19	53	58	2	59	1
10-a-92	7	106	681	0.16	33930	0.0487	0.0007	0.0694	0.0017	0.0103	0.0002	0.81	42	135	34	68	2	66	1
10-a-95	3	223	190	1.17	9495	0.0492	0.0015	0.0705	0.0025	0.0104	0.0002	0.54	29	159	69	69	2	67	1
[b]~~10-a-96~~	~~0~~	~~0~~	~~0~~	~~0.19~~	~~140~~	~~0.0918~~	~~0.1861~~	~~3.2628~~	~~6.5827~~	~~0.2578~~	~~0.0722~~	~~0.03~~	~~59~~	~~1463~~	~~1888~~	~~1472~~	~~948~~	~~1479~~	~~360~~
10-a-97	4	224	362	0.62	14967	0.0731	0.0016	0.0871	0.0025	0.0086	0.0002	0.67	5	1017	43	85	2	55	1
10-a-98	8	1087	486	2.24	24061	0.0466	0.0009	0.0662	0.0018	0.0103	0.0002	0.74	112	28	43	65	2	66	1
10-a-99	0	7	24	0.28	1292	0.0400	0.0059	0.0610	0.0090	0.0111	0.0003	0.10	28	-354	344	60	9	71	2
[b]~~10-a-101~~	~~0~~	~~1~~	~~10~~	~~0.07~~	~~479~~	~~0.0366~~	~~0.0106~~	~~0.0492~~	~~0.0141~~	~~0.0097~~	~~0.0004~~	~~0.03~~	~~8~~	~~-583~~	~~645~~	~~49~~	~~14~~	~~62~~	~~3~~
10-a-103	2	8	200	0.04	11471	0.0591	0.0014	0.0973	0.0030	0.0119	0.0003	0.63	12	572	52	94	3	77	2
10-a-104	3	227	165	1.38	129	0.0448	0.0008	0.0584	0.0015	0.0095	0.0002	0.74	3	-69	43	58	1	61	1
10-a-109	9	1247	636	1.96	27722	0.0472	0.0009	0.0594	0.0016	0.0091	0.0002	0.74	69	59	43	59	2	59	1
10-a-110	2	97	152	0.64	8557	0.0449	0.0016	0.0726	0.0029	0.0117	0.0003	0.48	248	-61	84	71	3	75	2
10-a-116	6	380	471	0.81	20609	0.0509	0.0012	0.0645	0.0020	0.0092	0.0002	0.63	22	237	55	63	2	59	1
[b]~~10-a-117~~	~~2~~	~~19~~	~~21~~	~~0.90~~	~~18~~	~~0.2108~~	~~0.0037~~	~~0.4873~~	~~0.0119~~	~~0.0168~~	~~0.0004~~	~~0.74~~	~~4~~	~~2912~~	~~28~~	~~403~~	~~8~~	~~107~~	~~2~~
Average of Th/U values				[a]1.02															

[a] Average of Th/U values.
[b] Omitted from age calculation because of high discordance.
[c] not calculated.

Table 7
Data table of the zircon Lu–Hf isotope data for the felsic sample D1a from the Mawat ophiolite. Location (N-35° 51. 24′) (E-45° 32. 55′).

Sample	176Hf/177Hf	2s	178Hf/177Hf	2s	176Lu/177Hf	2s	176Yb/177Hf	2s	176Hf/177Hf i	2s	eHf*	2s	Time (Ga)	Note
D1-G-3	0.282722	0.000017	1.467354	0.000011	0.000066	0.000001	0.002678	0.000023	0.28272	0.000017	-0.3	0.1	0.087	magmatic
D1-G-4	0.282509	0.000050	1.467376	0.000019	0.000664	0.000012	0.023215	0.000290	0.28251	0.000050	-8.1	1.8	0.078	magmatic
D1-G-5	0.282707	0.000020	1.467365	0.000012	0.000107	0.000000	0.004654	0.000033	0.28271	0.000020	-0.9	0.7	0.083	magmatic
D1-G-6	0.282685	0.000026	1.467341	0.000012	0.000666	0.000012	0.026078	0.000734	0.28268	0.000026	-1.6	0.9	0.091	magmatic
D1-G-7	0.282777	0.000020	1.467352	0.000013	0.000886	0.000008	0.028605	0.000350	0.28278	0.000020	1.5	0.7	0.082	magmatic
D1-G-8	0.282448	0.000031	1.467335	0.000019	0.001115	0.000053	0.034138	0.002079	0.28245	0.000031	-10.0	1.1	0.088	magmatic
D1-G-9	0.282547	0.000037	1.467419	0.000016	0.000081	0.000002	0.003077	0.000025	0.28255	0.000037	-6.6	1.3	0.081	magmatic
D1-G-10	0.282715	0.000018	1.467342	0.000011	0.000097	0.000001	0.004222	0.000021	0.28272	0.000018	-0.6	0.6	0.083	magmatic
D1-G-11	0.282785	0.000017	1.467331	0.000011	0.000605	0.000003	0.021929	0.000095	0.28278	0.000017	2.2	0.6	0.100	magmatic
average											-2.7			
std											4.4			
variation											11.5			

sample D1a (Table 7). The individual $^{206}Pb/^{238}U$ age was used for the calculation of the initial ε_{Hf} values since the zircon ages show a spread between 100 and 78 Ma The zircons yielded initial $^{176}Hf/^{177}Hf$ values between 0.28245 and 0.28278 corresponding to the initial ε_{Hf} values between -10 and +2.2 with an average value of -2.7. The zircons show $^{176}Lu/^{177}Hf < 0.0012$ and $^{176}Yb/^{177}Hf < 0.035$.

Two Hf isotope determinations were performed on two zircons from sample D3 (Table 8). For the calculation of the initial ε_{Hf} values, the individual $^{206}Pb/^{238}U$ ages (83 Ma and 70 Ma) were used. The zircons yielded initial $^{176}Hf/^{177}Hf$ values 0.28268 and 0.28262 corresponding to initial ε_{Hf} values of -4.4 and -1.7 with an average value of -3.1. The zircons show $^{176}Lu/^{177}Hf$ between 0.00086 and 0.00177 and $^{176}Yb/^{177}Hf$ between 0.02 and 0.04.

Seventeen Hf isotope determinations were performed on fourteen zircons from sample GB1 (Table 9). The individual $^{206}Pb/^{238}U$ age was used for the calculation of the initial ε_{Hf} values since the ages show a spread between 75-40 Ma. The seventeen analyses yielded initial $^{176}Hf/^{177}Hf$ values between 0.28265 and 0.28300 corresponding to initial ε_{Hf} values between - 3.3 and +9.1 with an average value of +3.5. The analyses exhibit homogeneous $^{176}Lu/^{177}Hf$ values between 0.0005-0.003 and $^{176}Yb/^{177}Hf$ values between 0.009-0.07.

5. Discussion

5.1. Age of the felsic dykes

The zircon data from both felsic dykes scatter widely hampering the evaluation of the zircon crystallisation ages. The common feature of the zircons is their high U contents (Tables 1, 2 and 4) which often lead to radiation damage of the crystals letting hydrothermal fluids enter the grains and disturb the U–Th–Pb system (e.g., Zhao et al., 2014 and references therein).

Textural features of the zircons are characterised by spongy domains, presence of pores and the intergrowth with minerals such as xenotime, monazite and other unidentified Th- and U-rich phases (Fig. 5A, B and H). Such textures can be produced in low temperature aqueous fluid-rich environment through a coupled dissolution-reprecipitation process (Tomaschek et al., 2003; Hay and Dempster, 2009). In a magmatic-hydrothermal system, hydrothermal zircon may precipitate, or magmatic zircon can be altered by aqueous fluids exsolved, e.g., from a granite (Schaltegger, 2007). Zircon in some hydrothermal environments can be easily altered by a fluid, causing secondary textures and chemical signatures on the primary zircon (Hoskin and Black, 2000; Corfu et al., 2003; Geisler et al., 2007; Park et al., 2016). In this study, the low Th/U ratios in the zircons (average 0.16) are compatible with the metamorphic (Hoskin and Schaltegger, 2003; Yakymchuk et al., 2018) or hydrothermal (Pettke et al., 2005) zircons.

When the size of the zircons allowed, several spots were placed on the same zircons in sample D1b. This revealed a within-grain large age variation, especially in grains 7 and 10 (Fig. 6C: Table 2). Pb loss is evident in many analyses (c.f., Corfu, 2013 and references therein), but the data also show reversely discordant analyses and older ages, i.e., apparent Pb gain (Fig. 6B). This phenomena has been referred to as redistribution (Mattinson et al., 1996) or mobilisation (Kusiak et al., 2013) of radiogenic Pb. In the ion imaging experiment on Archean zircons, Kusiak et al., (op.cit) found age variation between 2757 and 4150 Ma within the same grain. In the present study the grain number 10 shows the largest within-grain $^{206}Pb/^{238}U$ age variation; 83 Ma (slightly discordant) and 222 Ma (slightly reversely discordant).

The very low whole-rock Zr content in D1 and D3 (19.7 and 34.3 ppm) makes it hard for zircon to crystallise from such a melt (c.f., Watson, 1979). This evokes a process where inherited zircons were resolved in magma and the new zircons crystallise from the very same spots where necessary Zr was present. Memory of the old component may still reside in some grains. The negative ε_{Hf} values (see below) also suggest an older component in the magma source.

Table 8
Data table of the zircon Lu–Hf isotope data for the gabbro sample D3 from the Mawat ophiolite. Location (N-35° 50 41′) (E-45° 33 12′).

Sample	176Hf/177Hf	2s	178Hf/177Hf	2s	176Lu/177Hf	2s	176Yb/177Hf	2s	176Hf/177Hf i	2s	eHf*	2s	Time (Ga)
D3-Zr-50m-5Hz-5mJ-3.84cm2-14	0.282619	0.000021	1.467206	0.000014	0.00177	0.000009	0.03994	0.00032	0.28262	0.000021	-4.4	0.8	0.070
D3-Zr-50m-5Hz-5mJ-3.84cm2-15	0.282686	0.000018	1.467270	0.000014	0.00086	0.000003	0.02066	0.00011	0.28268	0.000018	-1.7	0.7	0.083
average											-3.0		
std											1.9		
variation											-2.7		

Table 9
Data table of the zircon Lu–Hf isotope data for the gabbro sample BG1 from the Mawat ophiolite. Location (N-35° 52 24′) (E-45° 33 11′).

Sample	176Hf/177Hf	2s	178Hf/177Hf	2s	176Lu/177Hf	2s	176Yb/177Hf	2s	176Hf/177Hf i	2s	eHf*	2s	Time (Ga)
MOCGB1a-50m-5Hz-4mJ-4.8jcm2-10	0.283003	0.000019	1.467159	0.000023	0.00031	0.00000	0.0055	0.0000	0.28300	0.000019	9.1	0.7	0.061
MOCGB1a-50m-5Hz-4mJ-4.8jcm2-28	0.282655	0.000044	1.467210	0.000037	0.00091	0.00001	0.0176	0.0003	0.28265	0.000044	-3.3	1.5	0.060
MOCGB1a-50m-5Hz-4mJ-4.8jcm2-30	0.282795	0.000040	1.467221	0.000024	0.00100	0.00004	0.0223	0.0013	0.28279	0.000040	1.7	1.4	0.063
MOCGb1a-50m-5Hz-4mJ-4.8jcm2-76	0.282914	0.000032	1.467195	0.000030	0.00157	0.00006	0.0357	0.0012	0.28291	0.000032	5.8	1.1	0.059
MOCGb1a-50m-5Hz-4mJ-4.8jcm2-77	0.282718	0.000022	1.467151	0.000030	0.00157	0.00002	0.0371	0.0004	0.28272	0.000022	-0.9	0.8	0.072
MOCGb1a-50m-5Hz-4mJ-4.8jcm2-77a	0.282825	0.000033	1.467253	0.000034	0.00143	0.00005	0.0343	0.0014	0.28282	0.000033	2.9	1.2	0.072
MOCGb1a-50m-5Hz-4mJ-4.8jcm2-86	0.282941	0.000023	1.467156	0.000026	0.00115	0.00001	0.0246	0.0003	0.28294	0.000023	6.7	0.8	0.053
MOCGB1a-50m-5Hz-4mJ-4.8jcm2-90	0.282776	0.000028	1.467153	0.000025	0.00061	0.00001	0.0128	0.0001	0.28278	0.000028	1.3	1.0	0.073
MOCGB1a-50m-5Hz-4mJ-4.8jcm2-92	0.282842	0.000019	1.467169	0.000021	0.00086	0.00001	0.0168	0.0002	0.28284	0.000019	3.5	0.7	0.066
MOCGb1a-50m-5Hz-4mJ-4.8jcm2-97	0.282887	0.000041	1.467142	0.000040	0.00193	0.00003	0.0404	0.0008	0.28289	0.000041	4.8	1.4	0.055
MOCGb1a-50m-5Hz-4mJ-4.8jcm2-99	0.282782	0.000029	1.467106	0.000039	0.00087	0.00002	0.0197	0.0006	0.28278	0.000029	1.4	1.0	0.071
MOCGb1a-50m-5Hz-4mJ-4.8jcm2-103	0.282899	0.000033	1.467216	0.000035	0.00053	0.00000	0.0095	0.0001	0.28290	0.000033	5.7	1.2	0.077
MOCGb1a-50m-5Hz-4mJ-4.8jcm2-111	0.282885	0.000041	1.467220	0.000032	0.00140	0.00003	0.0323	0.0007	0.28288	0.000041	5.1	1.4	0.075
MOCGb1a-50m-5Hz-4mJ-4.8jcm2-115	0.282806	0.000051	1.467128	0.000035	0.00048	0.00001	0.0097	0.0002	0.28281	0.000051	2.4	1.8	0.075
MOCGB1a-50m-5Hz-4mJ-4.8jcm2-n1	0.282805	0.000026	1.467180	0.000026	0.00078	0.00001	0.0180	0.0004	0.28280	0.000026	2.3	0.9	0.075
MOCGB1a-50m-5Hz-4mJ-4.8jcm2-n2	0.282939	0.000028	1.467191	0.000033	0.00290	0.00004	0.0689	0.0010	0.28294	0.000028	7.0	1.0	0.075
MOCGB1a-50m-5Hz-4mJ-4.8jcm2-n3	0.282866	0.000026	1.467182	0.000024	0.00172	0.00009	0.0466	0.0026	0.28286	0.000026	4.4	0.9	0.075
average											3.5		
std											3.1		
variation											-1.0		

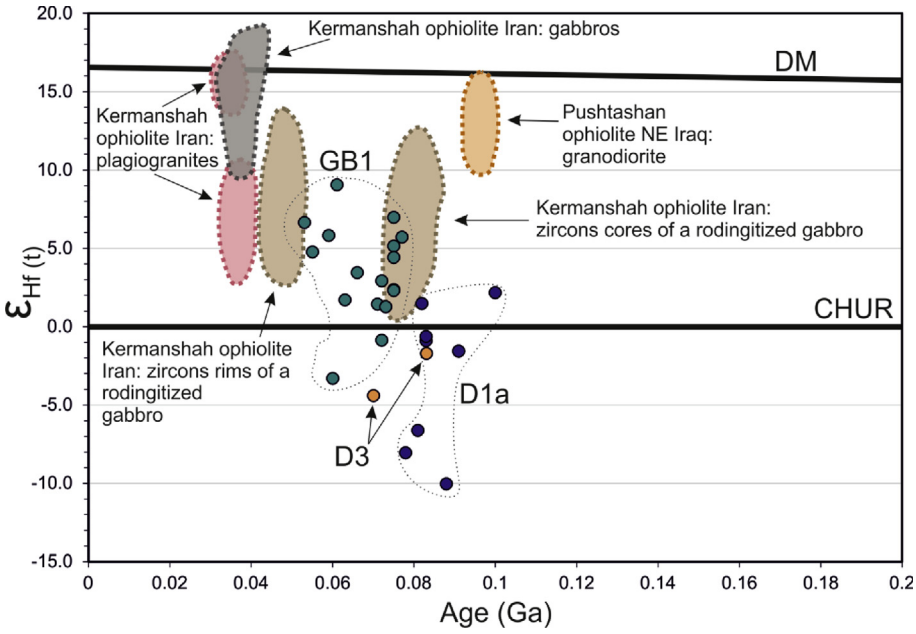

Fig. 7. ε_{Hf} vs age diagram for dykes D1a and D3 and gabbro GB1. Data from Pushtashan ophiolite, NE Iraq (Ismail et al., 2017) and Kermanshah ophiolite, Iran (Ao et al., 2016), are shown for comparison. CHUR = chondritic uniform reservoir (Bouvier et al., 2008); DM = Depleted Mantle (Griffin et al., 2000).

It is probable that monazite was crystallised directly from the felsic magma containing the necessary elements for monazite growth. Therefore the monazite in sample D1a gives the crystallisation age of the felsic magma. The age ~95 Ma is in good agreement with previous age determinations from the Daraban leucogranite in Mawat (96.8 ± 6.0 Ma zircon; 93.2 ± 1.7 Ma monazite and 94.6 ± 2.2 Ma xenotime; Mohammad and Qaradaghi, 2016; Mohammad et al., 2017), the Rb–Sr mineral isochron age of 93.4 ± 1.8 Ma (Azizi et al., 2013) and the nearby 96 ± 2 Ma Pushtashan throndhjemite (zircon; Ismail et al., 2017). Similar ages are also common throughout the Neo-Tethyan ophiolites (e.g., Moghadam and Stern, 2011 and references therein). However, the monazites in sample D3 also show younger ages of ~40 Ma, obviously affected a younger event (see below).

In summary, we infer that the ~95 Ma monazite in sample D1a dates the crystallisation of the felsic dyke D1. The oldest zircon from the same sample gives the same age within error, which we consider to represent the grain which has remained isotopically most closed during the subsequent modifications. The intergrowth of zircon and monazite also suggest simultaneous crystallisation. The monazite in dyke D3 is discordant but the zircon gives roughly the same ages than in D1. Consequently, the two dykes are considered coeval.

5.2. Age of the gabbro

The gabbro sample GB1 contains euhedral zircons that occasionally show oscillatory zoning. The Th/U ratios in zircons (average 1.02) are such found in zircons of igneous origin (Hoskin and Schaltegger, 2003; Kirkland et al., 2015). This suggests that the zircon saturated from the melt. However, the age data of 78 analyses show a semi-continuous range of concordia and $^{206}Pb/^{238}U$ ages between 81 and 38 Ma including discordant and reversely discordant analyses. The majority of the concordant and near concordant ages fall between 75 and 55 Ma (Fig. 6H, Table 6). The zircon contains BSE-dark spots of plagioclase and pyroxene and BSE-bright spots of Th- and U-rich phases. In this respect, the zircons resemble those found in the felsic dykes. Therefore, it is probable that these grains also were affected by a younger event causing the Pb loss probably combined with within-grain Pb mobility at ~40 Ma. We interpret the oldest 81 Ma age to show the crystallization age of the zircon and magma.

The age of the gabbro is > 10 Ma younger than the felsic dykes that crosscut the ultramafic mantle section. The 79.3 ± 0.9 Ma gabbroic magmatism is common in the Kermanshah ophiolite, about 250 km SE of Mawat. Ao et al. (2016) interpret them to be related to continental rifting forming the oceanic crust. If the gabbros in Kermanshah and in Mawat are the same, then Mawat has started to form much earlier than Kermanshah demonstrating the diachronic tectonic evolution in the Zagros Orogenic Belt. The Mawat gabbro has also been interpreted as rift-related to the extensional setting over the supra-subduction zone (Al Humadi et al., 2018b). Apparently, the 81 Ma gabbros are more common than so far recognised in the Zagros belt.

5.3. The youngest 40 Ma ages

A specific feature of the U–Pb data sets in both felsic and mafic samples is the wide range of zircon and monazite ages. As the zircon and monazite morphology in youngest and oldest grains within the same samples are similar, we interpret that all the grains are from the same generation. Many of the apparently concordant analyses follow the concordia line (Figs 6A-D and 6F–H), but as discussed by Corfu (2013), it can be a shortcoming of a short time gap between oldest and youngest analyses and the low resolution single analysis of the laser ablation method with large error ellipses overlapping each other and the concordia curve. Accepting this, the present data can be interpreted so that the oldest and youngest analyses form upper and lower intercepts, respectively, on the concordia curve. The youngest ages in all the three samples are ~40 Ma which we interpret as the time of Pb loss/mobilisation event. So what happened then?

There are many igneous rocks of that age in the region. A gabbro in the Bulfat ophiolite, 50 km north of Mawat, is 39 Ma (U–Pb zircon; Ali, 2017). ^{40}Ar -^{39}Ar hornblende and biotite also give 39 Ma indicating a rapid cooling at the time (Aswad et al., 2016). In the Kermanshah ophiolite a 39 Ma gabbro and a 36 Ma plagiogranite are dated (U–Pb zircon, Ao et al., 2016) and recently 41-39 Ma granites were described in the northern part of the Sanandaj-Sirjan zone (U–Pb zircon; Zhang et al.,

2018). Cenozoic magmatism is also common northeast of the Zagros belt (Dilek et al., 2010) about 50 km north of the Mawat ophiolite.

The ~40 Ma ages recorded in Mawat are probably related to these tectonic events even though they still are poorly known and controversial in detail. During the closure of the Neo-Tethyan ocean the crustal extension and related volcanism took place at 50–40 Ma in southeastern Turkey (Robertson et al., 2013). In Iran, extensional events evidenced in the late Paleocene to late Eocene with mid Eocene 54–40 Ma volcanism and plutonism (Verdel et al., 2011). The recent of 36 and 39 Ma rocks in the Kermanshah ophiolite evidence the presence of the Neo-Tethyan ocean in the late Eocene (Ao et al., 2016).

In the Mawat ophiolite, the Daraban granite has crystallised at 96.8 ± 6.0 Ma (Mohammad et al., 2016) while its ^{40}Ar -^{39}Ar muscovite age is 38 ± 1 Ma (Mohammad et al., 2014). They interpreted ~38 Ma to represent the beginning of the continental collision between the Arabian and Eurasian continents. The same conclusion was drawn from the similar ^{40}Ar -^{39}Ar ages from Bulfat (Aswad et al., 2016). So, there are two interpretations of the tectonic events at ~40 Ma. Perhaps advancing and retreating subduction generated both compressional and extensional events.

5.4. Lu–Hf data

The Lu–Hf isotope system in zircon is ideal to trace the source of the magma as the zircons used for U–Pb dating can be used to analyse *in-situ* ^{176}Lu/^{177}Hf and ^{176}Hf/^{177}Hf ratios in the same grains. The initial ratios inherited from the host at the time of zircon crystallisation are preserved in the grains unchanged provided that the system has remained closed. The ^{176}Hf/^{177}Hf ratio can be used to calculate the initial ε_{Hf} value which is a sensitive tool to infer whether the magma comes from an older (negative value) or juvenile (positive value) source (e.g., Kinny and Maas, 2003).

The two felsic dykes, D1 (zircon ages between 100 and 78 Ma) and D3 (83 and 70 Ma) have negative average initial ε_{Hf} values (- 2.7 and -3.1, respectively) with the lowest value of -10.0 (Fig. 7; Tables 7 and 8). Such negative values indicate that the source of the felsic magma is older than the intrusion age suggesting a crustal contribution. The wide range of values might indicate a heterogeneous or mixed source, or alternatively, later incomplete equilibration. The zircon grains from the gabbro GB1 (75-53 Ma), have positive average initial ε_{Hf} value of +3.5 with the highest value of +9.1 (Fig. 7; Table 9). This suggests that the magma was derived from a juvenile source. The average initial ε_{Hf} value in the nearby Pushtashan ophiolite is higher, +13.9 (Ismail et al., 2017). This may indicate that the Mawat gabbro comes from an older source or that it has contaminated with such a source.

6. Conclusions

The zircon and monazite ages from two felsic dykes crosscutting the mantle section of the Mawat ophiolite show a wide scatter on the concordia diagram forming an upper and lower intercepts of ~95 and ~40 Ma, respectively. Several processes are interpreted to cause the scatter including Pb loss and mobility of radiogenic Pb in the presence of fluids. ~95 Ma is interpreted to be the intrusion age of the dykes showing that the ultramafic host rocks are older. The zircon initial ε_{Hf} values are clearly negative pointing to an older source region for the felsic magma. The gabbro zircon ages also show a wide scatter with oldest zircons of ~81 Ma and the youngest of ~40 Ma. This younger mafic magmatism is located within the thrust zone and is interpreted to be related to extension, similar the coeval gabbros in the Kermanshah ophiolite. The youngest ~40 Ma zircons are found both in the felsic dykes and the gabbro. That age is common in the Zagros Orogenic Belt and is often referred to crustal extension during the Eocene or the time of collision. In Kermanshah the ocean was still open at the time demonstrating that the collision had not started yet or that the tectonism is highly diachronic.

Declarations

Author contribution statement

H. S. Al Humadi: Conceived and designed the experiments; Performed the experiments; Analyzed and interpreted the data; Contributed reagents, materials, analysis tools or data; Wrote the paper.

M. Väisänen: Analyzed and interpreted the data; Wrote the paper.

S. A. Ismail: Conceived and designed the experiments; Analyzed and interpreted the data; Contributed reagents, materials, analysis tools or data; Wrote the paper.

J. Kara, H. O'Brien, Y. Lahaye: Analyzed and interpreted the data; Contributed reagents, materials, analysis tools or data; Wrote the paper.

M. Lehtonen: Contributed reagents, materials, analysis tools or data.

Funding statement

This work was supported by The Ministry of High Education and Scientific Research of Iraq (33630/2014), The University of Babylon, Iraq and The University of Turku, Finland.(1/2017).

Competing interest statement

The authors declare no conflict of interest.

Additional information

No additional information is available for this paper.

Acknowledgements

Arto Peltola is thanked for making the zircon mounts and polished thin sections. Two anonymous reviewers are thanked for their constructive comments. This is the Finnish Geosciences Research Laboratory contribution.

References

Abbate, E., Bortolotti, V., Principi, G., 1980. Apennine ophiolites: a peculiar oceanic crust. Ofioliti 1, 59–96.

Agard, P., Monié, P., Gerber, W., Omrani, J., Molinaro, M., Meyer, B., Labrousse, L., Vrielynck, B., Jolivet, L., Yamato, P., 2006. Transient, synobduction exhumation of Zagros blueschists inferred from P-T, deformation, time, and kinematic constraints: implications for Neotethyan wedge dynamics. J. Geophys. Res.: Solid Earth 111 (B11).

Alavi, M., 1994. Tectonics of the Zagros orogenic belt of Iran: new data and interpretations. Tectonophysics 229, 211–238.

Aleinikoff, J.N., Schenck, W.S., Plank, M.O., Srogi, L., Fanning, C.M., Kamo, S.L., Bosbyshell, H., 2006. Deciphering igneous and metamorphic events in high-grade rocks of the Wilmington Complex, Delaware: morphology, cathodoluminescence and backscattered electron zoning, and SHRIMP U-Pb geochronology of zircon and monazite. Geol. Soc. Am. Bull. 118, 39–64.

Al Humadi, H., Väisänen, M., Ismail, S.A., 2018a. Geochemistry of mafic and ultramafic rocks from the Mawat ophiolite, NE Iraq. In: 4th National Colloquium of Geosciences, Turku, 14–15 March 2018. Geological Survey of Finland, p. 11. Abstract Book.

Al Humadi, H., Ismail, S.A., Väisänen, M., 2018b. Evidence of rifting over the supra subduction zone Mawat Ophiolite NE, Iraq: implication for late-stage gabbro formation. In: 8th Geochemistry Symposium, Antalya 2-6 May 2018. Karadeniz Technical University of Turkey, p. 96. Abstract Book.

Al-Kadhimi, J.A.M., Sissakian, V.K., Fattah, A.S., Deikran, D.B., 1996. Tectonic Map of Iraq. Geological Survey and Mining of Iraq, pp. 1–38.

Ali, S.A., Buckman, S., Aswad, K.J., Jones, B.G., Ismail, S.A., Nutman, A.P., 2012. Recognition of late cretaceous Hasanbag ophiolite-arc rocks in the kurdistan region of the Iraqi Zagros suture zone: a missing link in the paleogeography of the closing neotethys ocean. Lithosphere 4, 395–410.

Ali, S.A., Buckman, S., Aswad, K.J., Jones, B.G., Ismail, S.A., Nutman, A.P., 2013. The tectonic evolution of a neo-tethyian (Eocene-Oligocene) island-arc (Walash and naopurdan groups) in the kurdistan region of the northeast Iraqi Zagros suture zone. Isl. Arc 22, 104–125.

Ali, S.A., 2017. 39 Ma U-Pb zircon age for the Shaki-Rash gabbro in the Bulfat igneous complex, Kurdistan region, Iraqi Zagros Suture zone: rifting of an Intra-Neotethys Cenozoic arc. Ofioliti 42, 69–80.

Al-Qayim, B., Ibrahim, A., Koyi, H., 2012. Tectonostratigraphic overview of the Zagros suture zone, kurdistan, NE Iraq. GeoArabia 17, 109–115.

Ao, S., Xiao, W., Jafari, M.K., Talebian, M., Chen, L., Wan, B., Ji, W., Zhang, Z., 2016. U–Pb zircon ages, field geology and geochemistry of the Kermanshah ophiolite (Iran): from continental rifting at 79 Ma to oceanic core complex at ca. 36 Ma in the southern Neo-Tethys. Gondwana Res. 31, 305–318.

Arai, S., Shimizu, Y., Ismail, S.A., Ahmed, A.H., 2006. Low-T formation of high-Cr spinel with apparently primary chemical characteristics within podiform chromitite from Rayat, northeastern Iraq. Mineral. Mag. 70, 499–508.

Aswad, K.J., Elias, E.M., 1988. Petrogenesis, geochemistry and metamorphism of spilitized subvolcanic rocks of the Mawat Ophiolite Complex, NE Iraq. Ofioliti 13, 95–109.

Aswad, K.J., Aziz, N.R., Koyi, H.A., 2011. Cr-spinel compositions in serpentinites and their implications for the petrotectonic history of the Zagros Suture Zone, Kurdistan Region, Iraq. Geol. Mag. 148, 802–818.

Aswad, K.J., Ali, S.A., Sheraefy, R.M.A., Nutman, A.P., Buckman, S., Jones, B.G., Jourdan, F., 2016. 40Ar/39Ar hornblende and biotite geochronology of the Bulfat igneous complex, Zagros suture zone, NE Iraq: new insights on complexities of Paleogene arc magmatism during closure of the neotethys ocean. Lithos 266, 406–413.

Aziz, N.R.H., 2008. Petrogenesis, Evolution, and Tectonics of the Serpentinites of the Zagros Suture Zone, Kurdistan Region, NE Iraq. Ph. D. Thesis. University of Sulaimani, p. 250.

Azizi, H., Hadi, A., Asahara, Y., Mohammad, Y.O., 2013. Geochemistry and geodynamics of the Mawat mafic complex in the Zagros Suture zone, northeast Iraq. Cent. Eur. J. Geosci. 5, 523–537.

Belousova, E.A., O, W.L., Reilly, S.Y., 2006. Zircon crystal morphology, trace element signature and Hf isotope composition as a tool for petrogenetic modelling: example from eastern Australian granitoids. J. Petrol. 47, 329–353.

Bouvier, A., Vervoort, J.D., Patchett, P.J., 2008. The Lu-Hf and Sm-Nd isotopic composition of CHUR; constraints from unequilibrated chondrites and implications for the bulk composition of terrestrial planets. Earth Planet. Sci. Lett. 273, 48–57.

Chu, N.C., Taylor, R.N., Chavagnac, V., Nesbitt, R.W., Boella, R.M., Milton, J.A., Burton, K., 2002. Hf isotope ratio analysis using multi-collector inductively coupled plasma mass spectrometry: an evaluation of isobaric interference corrections. J. Anal. Atomic Spectrom. 17, 1567–1574.

Corfu, F., Hanchar, J.M., Hoskin, P.W., Kinny, P., 2003. Atlas of zircon textures. Rev. Mineral. Geochem. 53, 469–500.

Corfu, F., 2013. A century of U-Pb geochronology: the long quest towards concordance. Geol. Soc. Am. Bull. 125, 33–47.

Dercourt, J.E.A., Zonenshain, L.P., Ricou, L.-E., Kazmin, V.G., Le Pichon, X., Knipper, A.L., Grandjacquet, C., Sbortshikov, I.M., Geyssant, J., Lepvrier, C., Pechersky, D.H., Boulin, J., Sibuet, J.-C., Savostin, L.A., Sorokhtin, O., Westphal, M., Bazhenov, M.L., Lauer, J.P., Pechersky, D.H., 1986. Geological evolution of the tethys belt from the atlantic to the pamirs since the LIAS. Tectonophysics 123, 241–315.

Dilek, Y., Thy, P., Hacker, B., Grundvig, S., 1999. Structure and petrology of Tauride ophiolites and mafic dike intrusions (Turkey): implications for the Neotethyan Ocean. Geol. Soc. Am. Bull. 111, 1192–1216.

Dilek, Y., Furnes, H., Shallo, M., 2007. Suprasubduction zone ophiolite formation along the periphery of Mesozoic Gondwana. Gondwana Res. 11, 453–475.

Dilek, Y., Thy, P., 2009. Island arc tholeiitic to boninitic melt evolution of the Cretaceous Kizildag (Turkey) ophiolite: model for multi-stage early arc–forearc magmatism in Tethyan subduction factories. Lithos 113, 68–87.

Dilek, Y., Imamverdiyev, N., Altunkaynak, Ş., 2010. Geochemistry and tectonics of Cenozoic volcanism in the Lesser Caucasus (Azerbaijan) and the peri-Arabian region: collision-induced mantle dynamics and its magmatic fingerprint. Int. Geol. Rev. 52, 536–578.

Falcon, N.L., 1974. Southern Iran: Zagros mountains. In: Spencer, A.M. (Ed.), Mesozoic-Cenozoic Orogenic Belt: Data for Orogenic Studies, 4. Geological Society, London, Special Publications, pp. 199–211.

Geisler, T., Schaltegger, U., Tomaschek, F., 2007. Re-equilibration of zircon in aqueous fluids and melts. Elements 3, 43–50.

Gerdes, A., Zeh, A., 2006. Combined U-Pb and Hf isotope LA-(MC-) ICP-MS analysis of detrital zircons: comparison with SHRIMP and new constraints for the provenance and age of an Armorican metasediment in Central Germany. Earth Planet. Sci. Lett. 249, 47–61.

Griffin, W.L., Pearson, N.J., Belousova, E., Jackson, S.V., Van Achterbergh, E., O'Reilly, S.Y., Shee, S.R., 2000. The Hf isotope composition of cratonic mantle: LAM-MC-ICPMS analysis of zircon megacrysts in kimberlites. Geochem. Cosmochim. Acta 64, 133–147.

Hacker, B.R., 1994. Rapid emplacement of young oceanic lithosphere: argon geochronology of the man ophiolite. Science 265, 1563–1565.

Hassanzadeh, J., Wernicke, B.P., 2016. The Neotethyan Sanandaj-Sirjan zone of Iran as an archetype for passive margin-arc transitions. Tectonics 35, 586–621.

Hay, D.C., Dempster, T.J., 2009. Zircon behaviour during low-temperature metamorphism. J. Petrol. 50, 571–589.

Hessami, K., 2002. Tectonic History and Present-Day Deformation in the Zagros Fold-Thrust Belt. Uppsala University Doctoral dissertation, Ph. D. thesis.

Hoskin, P.W.O., Black, L.P., 2000. Metamorphic zircon formation by solid-state recrystallization of protolith igneous zircon. J. Metamorph. Geol. 18, 423–439.

Hoskin, P.W., Schaltegger, U., 2003. The composition of zircon and igneous and metamorphic petrogenesis. Rev. Mineral. Geochem. 53, 27–62.

Huhma, H., Mänttäri, I., Peltonen, P., Kontinen, A., Halkoaho, T., Hanski, E., Hokkanen, T., Hölttä, P., Juopperi, H., Konnunaho, J., Lahaye, Y., Luukkonen, E., Pietikäinen, K., Pulkkinen, A., Sorjonen-Ward, P., Vaasjoki, M., Whitehouse, M., 2012. The age of the Archaean greenstone belts in Finland. Geological Survey of Finland, Special Paper 54, 74–175.

Ismail, S.A., Al-Chalabi, S.A., 2006. Genesis of chromitite in qalander area, northern Iraq. Kirkuk University Journal for Scientific Studies 1, 10–29.

Ismail, S.A., Carr, P.F., 2008. A brief review of ophiolites in Iraq. In: International Symposia on Geoscience Resources and Environments of Asian Terranes (GREAT 2008), 4th IGCP 516, and 5th APSEG; November 24-26, 2008, p. 60. Bangkok, Thailand. Abstract Book.

Ismail, S.A., Arai, S., Ahmed, A.H., Shimizu, Y., 2009. Chromitite and peridotite from Rayat, northeastern Iraq, as fragments of a Tethyan ophiolite. Isl. Arc 18, 175–183.

Ismail, S.A., Mirza, T.M., Carr, P.F., 2010. Platinum-group elements geochemistry in podiform chromitites and associated peridotites of the Mawat ophiolite, northeastern Iraq. J. Asian Earth Sci. 37, 31–41.

Ismail, S.A., Kettanah, Y.A., Chalabi, S.N., Ahmed, A.H., Arai, S., 2014. Petrogenesis and PGE distribution in the Al-and Cr-rich chromitites of the Qalander ophiolite, northeastern Iraq: implications for the tectonic environment of the Iraqi Zagros Suture Zone. Lithos 202, 21–36.

Ismail, S.A., Ali, S.A., Nutman, A.P., Bennett, V.C., Jones, B.G., 2017. The Pushtashan juvenile suprasubduction zone assemblage of Kurdistan NE Iraq: a Cretaceous (Cenomanian) Neo-Tethys missing link. Geosci. Front. 8, 1073–1087.

Jassim, S.Z., Goff, J.C. (Eds.), 2006. Geology of Iraq. Brno, Czech Republic. Dolin, Prague and Moravian Museum, 341p.

Kara, J., Väisänen, M., Johansson, A., Lahaye, Y., O'Brien, H., Eklund, O., 2018. 1.90–1.88 Ga arc magmatism of central Fennoscandia: geochemistry, U-Pb geochronology, Sm-Nd and Lu-Hf isotope systematics of plutonic-volcanic rocks from southern Finland. Geol. Acta 16, 1–23.

Kinny, P.D., Maas, R., 2003. Lu–Hf and Sm–Nd isotope systems in zircon. Rev. Mineral. Geochem. 53, 327–341.

Kirkland, C.L., Smithies, R.H., Taylor, R.J.M., Evans, N., McDonald, B., 2015. Zircon Th/U ratios in magmatic environs. Lithos 212, 397–414.

Kusiak, M.A., Whitehouse, M.J., Wilde, S.A., Nemchin, A.A., Clark, C., 2013. Mobilization of radiogenic Pb in zircon revealed by ion imaging: implications for early Earth geochronology. Geology 41, 291–294.

Lagabrielle, Y., Cannat, M., 1990. Alpine Jurassic ophiolites resemble the modern central Atlantic basement. Geology 18, 319–322.

Ludwig, K.R., 2003. User's manual for isoplot/ex, version 3.00. A geochronological toolkit for microsoft excel. Berkeley Geochronology Centre Special Publication 4, 25–32.

Mattinson, J.M., Graubard, C.M., Parkinson, D.L., McClelland, W.C., 1996. U-Pb reverse discordance in zircons: the role of fine-scale oscillatory zoning and sub-micron transport of Pb. American Geophysical Union, Geophysical Monograph 95, 355–370.

Mirza, T.A., Ismail, S.A., 2007. Origin of plagiogranite in the Mawat ophiolite complex, kurdistan region, NE Iraq. Journal of Kirkuk University-Scientific Studies 2, 1–25.

Moghadam, H.S., Stern, R.J., Rahgoshay, M., 2010. The Dehshir ophiolite (central Iran): geochemical constraints on the origin and evolution of the Inner Zagros ophiolite belt. Geol. Soc. Am. Bull. 122, 1516–1547.

Moghadam, H.S., Stern, R.J., 2011. Geodynamic evolution of Upper Cretaceous Zagros ophiolites: formation of oceanic lithosphere above a nascent subduction zone. Geol. Mag. 148, 762–801.

Moghadam, H.S., Stern, R.J., 2014. Ophiolites of Iran: keys to understanding the tectonic evolution of SW Asia: (I) Paleozoic ophiolites. J. Asian Earth Sci. 91, 19–38.

Moghadam, H.S., Stern, R.J., 2015. Ophiolites of Iran: keys to understanding the tectonic evolution of SW Asia: (II) Mesozoic ophiolites. J. Asian Earth Sci. 100, 31–59.

Mohajjel, M., Fergusson, C.L., Sahandi, M.R., 2003. Cretaceous–Tertiary convergence and continental collision, Sanandaj–Sirjan zone, western Iran. J. Asian Earth Sci. 21, 397–412.

Mohammad, Y.O., Cornell, D.H., Qaradaghi, J.H., Mohammad, F.O., 2014. Geochemistry and Ar-Ar muscovite ages of the daraban leucogranite, Mawat ophiolite, northeastern Iraq: implications for arabia–eurasia continental collision. J. Asian Earth Sci. 86, 151–165.

Mohammad, Y.O., Qaradaghi, J.H., 2016. Geochronological and mineral chemical constraints on the age and formation conditions of the leucogranite in the Mawat ophiolite, Northeastern of Iraq: insight to sync-subduction zone granite. Arabian Journal of Geosciences 9, 608.

Mohammad, Y.O., Cornell, D.H., 2017. U–Pb zircon geochronology of the Daraban leucogranite, Mawat ophiolite, Northeastern Iraq: a record of the subduction to collision history for the Arabia–Eurasia plates. Isl. Arc 26, e12188.

Monsef, I., Monsef, R., Mata, J., Zhang, Z., Pirouz, M., Rezaeian, M., Esmaeli, R., Xiao, W., 2018. Evidence for an early-MORB to fore-arc evolution within the Zagros suture zone: constraints from zircon U-Pb geochronology and geochemistry of the Neyriz ophiolite (South Iran). Gondwana Res. 62, 287–305.

Morel, M.L.A., Nebel, O., Nebel-Jacobsen, Y.J., Miller, J.S., Vroon, P.Z., 2008. Hafnium isotope characterization of the GJ-1 zircon reference material by solution and laser-ablation MC-ICPMS. Chem. Geol. 255, 231–235.

Park, C., Song, Y., Chung, D., Kang, I.M., Khulganakhuu, C., Yi, K., 2016. Recrystallization and hydrothermal growth of high U–Th zircon in the Weondong deposit, Korea: record of post-magmatic alteration. Lithos 260, 268–285.

Parlak, O., Yilmaz, H., Boztuğ, D., 2006. Origin and tectonic significance of the metamorphic sole and isolated dykes of the Divriği ophiolite (Sivas, Turkey): evidence for slab break-off prior to ophiolite emplacement. Turk. J. Earth Sci. 15, 25–45.

Patchett, P., Tatsumoto, M., 1981. Lu/Hf in chondrites and definition of a chondritic hafnium growth curve. Lunar Planetary Science 12, 822–824.

Pearce, J.A., 1980. Geochemical evidence for the genesis and eruptive setting of lavas from Tethyan ophiolites. Proceedings of the International Ophiolite Symposium, Cyprus 1979. Ministry of Agriculture and Natural Resources, Cyprus, pp. 261–272.

Pettke, T., Audétat, A., Schaltegger, U., Heinrich, C.A., 2005. Magmatic-to-hydrothermal crystallization in the W–Sn mineralized Mole Granite (NSW, Australia): Part II: evolving zircon and thorite trace element chemistry. Chem. Geol. 220, 191–213.

Rahmani, F., Noghreyan, M., Khalili, M., 2007. Geochemistry of sheeted dikes in the Nain ophiolite (Central Iran). Ofioliti 32, 119–129.
Robertson, A.H., Parlak, O., Ustaömer, T., 2013. Late Palaeozoic–Early Cenozoic tectonic development of Southern Turkey and the easternmost Mediterranean region: evidence from the interrelations of continental and oceanic units. Geological Society, London, Special Publications 372, 372-22.
Rollinson, H., 2015. Slab and sediment melting during subduction initiation: granitoid dykes from the mantle section of the Oman ophiolite. Contrib. Mineral. Petrol. 170, 32.
Rosa, D.R.N., Finch, A.A., Andersen, T., Inverno, C.M.C., 2009. U-Pb geochronology and Hf isotope ratios of Magmatic zircons from the Iberian Pyrite Belt. Mineral. Petrol. 95, 47–69.
Schaltegger, U., 2007. Hydrothermal zircon. Elements 3, 51–79.
Scherer, E., Münker, C., Mezger, K., 2000. Lu-Hf garnet geochronology: closure temperature relative to the Sm-Nd system and the effects of the trace mineral inclusions. Geochem. Cosmochim. Acta 46, 3413–3432.
Sláma, J., Košler, J., Pedersen, R.B., 2007. Behaviour of zircon in high-grade metamorphic rocks: evidence from Hf isotopes, trace elements and textural studies. Contrib. Mineral. Petrol. 154, 335–356.
Smith, A.G., 1993. Tectonic significance of the Hellenic-Dinaric ophiolites. Geological Society, London, Special Publications 76, 213–243.
Söderlund, U., Patchett, P.J., Vervoort, J.D., Isachsen, C.E., 2004. The 176 Lu decay constant determined by Lu-Hf and U-Pb isotope systematics of Precambrian mafic intrusions. Earth Planet. Sci. Lett. 291, 311–324.
Tomaschek, F., Kennedy, A.K., Villa, I.M., Lagos, M., Ballhaus, C., 2003. Zircons from Syros, Cyclades, Greece -recrystallization and mobilization of zircon during high-pressure metamorphism. J. Petrol. 44, 1977–2002.
Van Achterbergh, E., Ryan, C., Jackson, S., Griffin, W., 2001. Appendix 3 Data reduction software for LA-ICP-MS. In: Sylvester, P. (Ed.), Laser-Ablation-Icpms in the Earth Sciences, Mineralogical Association of Canada. Short Course, 239-243.
Verdel, C., Wernicke, B.P., Hassanzadeh, J., Guest, B., 2011. A Paleogene extensional arc flare-up in Iran. Tectonics 30, 3.
Vervoort, J.D., Patchett, P.J., Söderlund, U., Baker, M., 2004. The isotopic composition of Yb and the determination of Lu concentrations and Lu/Hf ratios by isotope dilution using MC-IPCMS. Geochem. Geophys. Geosyst. 5, Q11002.
Watson, E.B., 1979. Zircon saturation in felsic liquids: experimental results and applications to trace element geochemistry. Contrib. Mineral. Petrol. 70, 407–419.
Yakymchuk, C., Kirkland, C.L., Clark, C., 2018. Th/U ratios in metamorphic zircon. J. Metamorph. Geol. 36, 715–737.
Zhang, Z., Xiao, W., Ji, W., Majidifard, M.R., Rezaeian, M., Talebian, M., Xiang, D., Chen, L., Wan, B., Ao, S., Esmaeili, R., 2018. Geochemistry, zircon U-Pb and Hf isotope for granitoids, NW Sanandaj-Sirjan zone, Iran: implications for Mesozoic-Cenozoic episodic magmatism during Neo-Tethyan lithospheric subduction. Gondwana Res. 62, 227–245.
Zhao, K.D., Jiang, S.Y., Ling, H.F., Palmer, M.R., 2014. Reliability of LA-ICP-MS U-Pb dating of zircons with high U concentrations: a case study from the U-bearing Douzhashan Granite in South China. Chem. Geol. 389, 110–121.